UC Irvine
UC Irvine Previously Published Works

Title

A general-purpose tool for modeling multifunctional thin porous media (POREnet): From pore network to effective property tensors.

Permalink

Journal

ISSN

Authors

García-Salaberri, Pablo

Zenyuk, Iryna

Publication Date

DOI

Peer reviewed
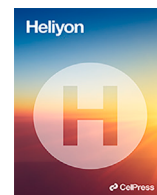
Research article

A general-purpose tool for modeling multifunctional thin porous media (*POREnet*): From pore network to effective property tensors

Pablo A. García-Salaberri [a],[*], Iryna V. Zenyuk [b]

[a] *Department of Thermal and Fluids Engineering, Universidad Carlos III de Madrid, Leganés 28911, Spain*
[b] *Department of Chemical & Biomolecular Engineering, National Fuel Cell Research Center, University of California Irvine, Irvine, CA 92697, USA*

ARTICLE INFO

ABSTRACT

POREnet, a novel approach to model effective properties of thin porous media, TPM, is presented. The methodology allows the extraction of local effective property tensors by volume averaging from discrete pore networks, PNs, built on the tessellated continuum space of a TPM. The gradient theorem is used to describe 3D transport in bulk tessellated space, providing an appropriate metric to normalize network fluxes. Implemented effective transport properties include diffusivity, permeability, solid-phase conductivity, and entry capillary pressure and contact angle under two-phase conditions, considering multi-component materials with several solid phases and local contact resistances. Calculated property tensors can be saved on 3D image stacks, where interfacial and sub-CV scale features can be added before exporting data to CFD meshes for simulation. Overall, *POREnet* provides a general-purpose, versatile methodology for modeling TPM in an ample range of conditions within a single CFD framework. Among other advantages, coupling of PN and continuum models at TPM-channel interfaces is simplified, interfacial contact resistances can be included using robin boundary conditions, and transient multiphysics simulations can be implemented more easily using CFD. The code is tested against a miscellaneousness of examples extracted from electrochemical applications.

1. Introduction

Thin porous media (TPM) play a key role in multiple applications, such as filters, papers, textiles, composite reinforcements, membranes and (reactive) transport layers [1]. By definition, TPM encompass porous materials whose thickness in the through-plane direction (TP) is significantly shorter than any in-plane (IP) length within the material plane. For this reason, TPM typically suffer from a lack of length scale separation between pore and layer scales in the TP direction, which barely spans a few pore sizes (see, e.g., [2,3]). Moreover, TPM are frequently used as a stack of porous layers, leading to inhomogeneous, deformable interfaces, manufacturing defects (e.g., cracks and holes) and interfacial regions (e.g., interpenetration of a macroporous layer and a microporous layer). The situation is more challenging for multifunctional TPM, such as those found in electrochemical energy devices (gas diffusion layers (GDLs), porous flow distributors, catalyst layers (CLs), membranes and macroporous electrodes) [4–8]. These TPM must fulfill multiple functions, simultaneously providing a route for gas/liquid reactant and product transport, charge transport and heat transport [2,9,10]. In addition, CLs and macroporous electrodes must provide an active surface area [11–15]. Optimal design and manufacturing of TPM at small scales ranging from nanometers to millimeters poses a non-trivial problem due to

the existence of usually conflicting effects in the targeted properties. For example, porous transport layers with high mass diffusivity require high porosity, but an exceedingly high porosity can lead to poor mechanical, thermal or electrical properties [2,10,16]. The interplay between microstructural properties (porosity, solid volume fraction, pore size, specific surface area, etc.) on the resulting effective transport properties (diffusivity, permeability, capillary resistance, electrical and thermal conductivities, etc.) is difficult to be anticipated [3,7,14,17].

A large body of work has been devoted to TPM modeling with industrial application (see, e.g., [1,18] and references therein). Generally speaking, modeling transport in TPM poses the opposite scenario to that found in pseudo-infinite PM (e.g., sand and rock reservoirs), where a representative elementary volume (REV) can usually be defined and macroscopic transport modeled at the (previously defined) REV scale [19,20]. The finite thickness that characterizes a TPM allows the modeler to describe macroscopic transport in the full thickness over a rather large area. However, the effect of a weak REV definition introduces uncertainty in the model formulation and numerical prediction [2,3,21]. It is not easy for the modeler to establish a general mathematical formulation for TPM with well-defined, measurable constitutive relationships that could describe the effect of intra and interlayer microstructural features on internal transport processes in any situation (with say less than 5% error) [17,22,23]. For example, a persistent problem of Darcian macroscopic models is the accurate prediction of two-phase capillary transport in TPM due to the dominant role of invasion-percolation (IP) processes, which are overlooked in a standard macro-homogeneous formulation [21]. As a result, the combination of macroscopic and microscopic modeling techniques, such as direct numerical simulation (DNS) and pore network modeling (PNM), is a widespread approach adopted to analyze TPM and extract more predictive results [5,24]. The combined use of macroscopic and microscopic information can be carried out in different ways using one-way micro-to-macro models, where effective transport properties determined from a numerical or analytical pore-scale model are plugged into a macroscopic model (see, e.g., [25–27]). And hybrid models, where microscopic and macroscopic formulations are combined simultaneously (e.g., DNS+macroscopic [28,29], PNM+macroscopic [11,16,30–34], continuum microscopic+macroscopic [35], or a combination thereof).

Pore-scale PN methods require a significantly lower computational effort than DNS at the cost of reduced microstructural resolution. Structural and morphological features below the pore-throat scale must be incorporated as part of pore-scale constitutive relationships (e.g., entry capillary pressure of throats or saturation retention curve of pores). This is a reasonable assumption in most engineering applications, where a trade-off between spatial resolution and numerical domain size is needed. For instance, DNS (e.g., lattice Boltzmann method, LBM [36]) can be used to perform more detailed simulations and extract constitutive relationships for PNM [37–39]. Thus, PN-based methods offer a simplified bridge-like framework between microscopic and macroscopic scales.

PNM was first introduced in the 50s by Fatt [40], as a more realistic alternative to bundle-of-tubes models, in tandem with the appearance of first computers. PNM offered a novel approach to analyze and understand transport in PM, which included cross-connections and tortuosity of the pore space in agreement with the analyses of other authors, such as Kozeny [41] and Carman [42]. During the second half of the 20th century, the interest of the community on versatile PN methods gradually increased hand in hand with the increase of computational performance. Significant contributions were presented by Dullien [43,44], Wilkinson [45], Prat [46,47], Blunt [48,49] and co-workers, just to name a few. More elaborated PN models were developed in 3D with different structures and topologies (compared to the rudimentary but pioneering 2D model of Fatt [40]). The use of PNM was not only restricted to the description of drainage and imbibition but applied to other physical processes (e.g., foam flow [50], non-Darcian effects in high-speed gas flows [51], evaporation/condensation [52], etc.). From the last decade of the 20th century, a strong growth in the use of PNM has taken place, mainly with a focus on petroleum and environmental science [48,53–56]. Multi-network dual and trial PN models (D-PNM and T-PNM) have been extensively presented to examine transport in multiscale PMs with a variable number of solid phases (e.g., transport in carbonate rocks [57], fractured vuggy reservoirs [58], hierarchical catalysts [59], membrane electrode assemblies (MEAs) [31–33], and battery electrodes [60]). Furthermore, significant progress has been achieved in the combination of PNM with X-ray computed tomography (X-CT) and virtually reconstructed PMs [57,61,62]. The continuous advancement in multiscale imaging techniques (nano and micro X-CT) and development of commercial and open-source computational tools for PM generation [63,64] provides a good complement for better description of complex microstructures [65–68].

The recent work on multi-network PN methods has also motivated the implementation of hybrid PNM and continuum models to capture small scales that can be difficult to reproduce only using PNM (e.g., effect of internal fractures and multi-component composition [58]) or to couple formulations between regions featuring different physical descriptions (e.g., coupling of PNM with a free flow formulation in a channel [69,70]). The main difficulty of hybrid models usually relies on the coupling of discrete and continuum formulations at boundary pores [71]. Several approaches have been proposed in the literature for scalar and flux continuity. Balhoff et al. [72] (2007) presented a single-phase flow model, which coupled a semi-analytical continuum formulation with a PNM, considering domains with a simple parallelepipedal geometry. Flux continuity at the shared boundary interface was enforced by solving for the coefficients of an analytical series expansion used to describe the continuum region. In a subsequent work, Balhoff et al. [73] (2008) presented a fully numerical hybrid PNM/continuum model, which relayed for the first time on 2D finite-element mortars to couple the solution of independent PM sub-domains. Mortar space is useful to enforce continuity of pressure and flux using a domain decomposition approach, since the numerical solution in the decomposed sub-domains can be calculated in parallel. However, the implementation can be tedious and can lead to complicated parallelization when the number of subdomains is large and they have a complex geometry, as it is the case of multiscale, multi-component TPM (e.g., CL). Mortars are potentially more useful when a single method is used to model transport in a full PM subdomain, including all its porous and multi-component features [74].

Later, Chu et al. [75] (2012) presented a hybrid algorithm, where transport in a PN model was locally coupled to an effective continuum conservation law upon average flux conservation. This modeling approach allowed to upscale information from a lower spatial scale resolved by PNM to an upper spatial scale given by the continuum, which could in turn be connected to other macro-

scopic continuum regions or a combination thereof. Liu et al. [67,68] (2021) used a conceptually similar approach to that presented by Chu et al. [75] but coupling pore-scale DNS with an effective continuum scale. The multiscale model was used to analyze reaction-diffusion transport through the combination of nano and micro X-CT of Pt-free CLs. The main complication of the above upscaling methods relies on their elaborated implementation for arbitrary 3D meshes, upscaling of discrete multiphase transport processes (e.g., IP [45]), integration of coupled multi-component transport processes between scales, and parallelization. In 2016-2017, Aghighi et al. [32] (2016) and Belgacem et al. [33] (2017) presented independently a hybrid PNM/continuum model of a polymer electrolyte membrane fuel cell (PEMFC) MEA. PNM was used to model transport in macroporous layers and a macro-homogeneous formulation to model transport in porous layers with fine pore sizes (microporous layers (MPLs), CLs and membrane). Aghighi et al. [32] (2016) coupled PNM pores and numerical continuum nodes using a finite difference method on a structured Cartesian mesh, so that PNM and continuum formulations could be both expressed as a resistor network and solved together iteratively (1 pore was connected to 25 continuum nodes). No need of complex coupling techniques based on mortars were needed. In contrast, Belgacem et al. [33] (2017) imposed interfacial coupling by means of a finite volume method on a structured Cartesian mesh (1 fluid/solid throat was connected to 1 continuum node). The similar form of PNM and finite volume formulations also allowed for a direct coupling of discretized equations between porous layers. As an alternative to hybrid models, Zhang et al. [58] (2017) presented a multiscale finite element method (MsFEM), where sub-grid scale heterogeinities and interaction through multiscale basis functions were calculated based on a multi-continuum background. Several 2D examples of a matrix-fracture-vug triple-continuum were examined, showing good agreement between multiscale and fine scale simulations (error lower than 5%). MsFEM methods are a promising multiscale approach, even though 3D widespread codes are still not available and little work has been performed on transient, multiphysics, continuum-discrete multiphase problems.

The above literature survey shows the growing effort devoted toward the development of comprehensive methods for the analysis of multi-component, multiscale PMs. The aim of this work is to present a novel, general-purpose method, *POREnet*, for extracting local effective transport properties from a tessellated PN representation of multifunctional TPM. The method is based on the previous work of García-Salaberri [10] on structured networks embedded in Cartesian CFD meshes but extended for control volumes (CVs) of arbitrary shape. In its current form, *POREnet* has been implemented in Matlab due to the wide availability of predefined tools. A sample code can be downloaded here. Unlike other methods, local effective transport properties can be directly included in a conventional CFD software for numerical simulation of transient, multiphysics processes (e.g., ANSYS, COMSOL Multiphysics, STAR-CCM+, OpenFOAM, etc.). This versatile, user-friendly framework simplifies the incorporation of pore-scale information into continuum models, providing an alternative approach to fully PN models [76]. Extracted effective transport properties could also be used as an input for multiscale continuum models (e.g., MsFEM [58]). Other advantages of the methodology include easier numerical implementation of comprehensive models of TPM and interfacial robin boundary conditions, especially when a PM is composed of many complex-shaped subdomains, and facilitated parallelization, since it is given by the simulation software and not affected by the coupling method between PNM-continuum formulations (e.g., mortars [73]). Regarding multiphase flow, the proposed method allows the extraction of local entry capillary pressures and contact angles of throats. This pore-scale information can be used to build multiphase models in CFD codes, e.g., continuum bundle-of-tubes models [77,78] or discrete PNM algorithms [16,30]. It is worth noting that the present approach is not exclusively restricted to TPM but could also be applied to other PM (e.g., transport in multiscale carbonate reservoirs and fractured rocks, flow near a well, etc.) or to extract properties for the description of larger PM systems (e.g., geothermal processes through stratified reservoirs, aquifers, etc.).

The organization of the work is as follows. In Section 2, the methodology used for the generation of continuum, tessellated CV assemblies with embedded discrete networks is presented, including both fluid and multi-component solid phases. In Sections 3 and 4, the method developed in *POREnet* to extract local microstructural properties (porosity, average pore size, specific surface area, etc.) and local effective transport properties (diffusivity, permeability and solid-phase conductivity) of TPM is presented. In Section 5, the flow chart of the implementation methodology is examined, with a focus on the main features included in the current version of *POREnet*. In Section 6, the modeling capabilities of *POREnet* are tested against a miscellaneousness of cases related with TPM, which were extracted from electrochemical applications. In Section 7, the limitations of the method are discussed. Finally, the concluding remarks and future work are given in Section 8.

2. Tessellation and network generation

2.1. Control volume tessellation of continuum space

Multiple mathematical algorithms exist for space tessellation in 2D and 3D, such as rectangular, triangular, pentagonal, octahedral or tetrahedral tiling, among others [79–82]. In this work, Voronoi tessellation was used for CV generation due to the large availability of fast algorithms already implemented in commercial and open-source codes. The *voronoin* function (from the C++ code *Qhull*) was used to determine Euclidean Voronoi diagrams in n-D space. For a prescribed set of 3D seed points, Voronoi diagrams provide a full space tessellation composed of convex polyhedral CVs, where each CV contains a single seed point. Faces dividing polyhedral CVs are equidistant to neighboring seed points, so that the distance of all points in a polyhedron to its owner seed point is lower than the distance to any other seed point. CV density can be modified by the distribution of seed points in 3D space.

As shown in Fig. 1(a)-(b), ordered rectangular tessellations can be simply generated using seed points with a fixed spacing in x, y, z-direction, $[\Delta L_x^\circ, \Delta L_y^\circ, \Delta L_z^\circ]$, so the centroid of any CV matches the corresponding seed point – reflection of Voronoi seed points is commonly used to control edge definition in polyhedral mesh generators [83]. Graded ordered tessellations can also be generated using an uneven but ordered spacing with *meshgrid*. Starting from an ordered tessellation, creation of a random distribution
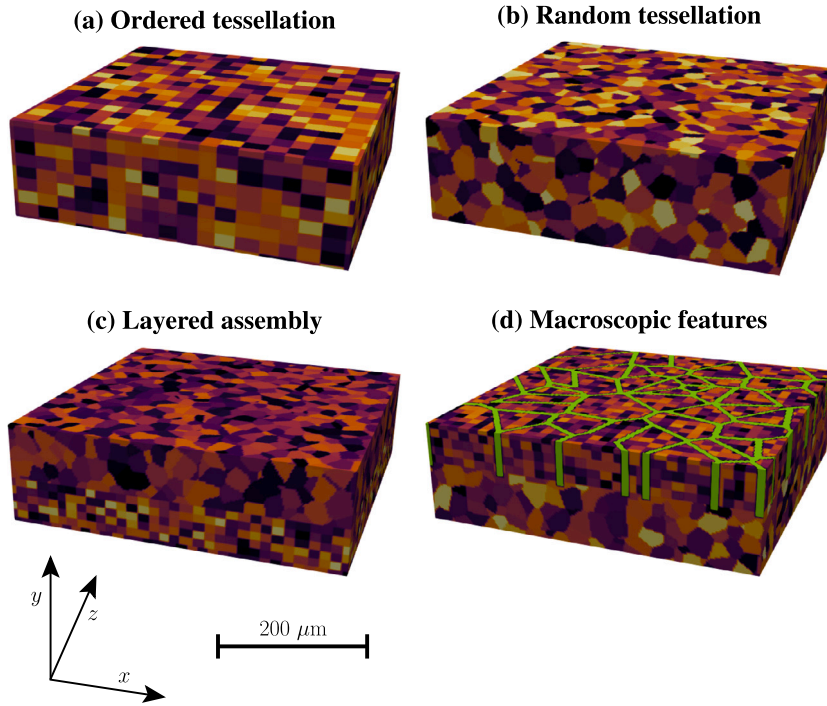
Fig. 1. (up) Ordered and random spatial tessellations generated from Voronoi diagrams with (a) equally spaced and (b) random seed points, respectively. (down) Compositions of different spatial tessellations in (c) a layered assembly and (d) a layered assembly with macroscopic features highlighted in green (cracks). The resolution of the output tif image stack is 5 μm.

of polyhedral CVs can be accomplished by perturbing the ordered seed points in the range $(L_i^\circ - \Delta L_i^\circ/2, L_i^\circ + \Delta L_i^\circ/2)$ for $i = x, y, z$. Alternatively, seed points can be extracted from X-CT images to reproduce more complex pore distributions (e.g., fibrous carbon cloths [84,85]). Often, boundary cells are problematic because they do not match the modeled finite-size domain. Issues with boundary cells can be overcome using an oversized "background PM", which extends a distance δ_i beyond the targeted domain. Adding two extra seed points in each direction, $\delta_i = 2\Delta L_i^\circ$, is enough to ensure that the targeted domain is fully covered of Voronoi cells without including vertices at infinity.

Other interior TPM regions can be superimposed on the "background PM" by sequentially adding data on a same matrix. Ultimately, data can be stored in a 3D image stack (e.g., Tif stack). For interior TPM regions, only CVs that lie inside the convex hull of a predefined bounding box are processed – the contributed *inhull* function [86] was used here. Unlike fully discrete PN methods, the sequential addition of tessellated TPM regions on image stacks provides a customizable approach to reproduce layered, multiscale TPM assemblies with or without interfacial regions and macroscopic defects. Fig. 1(c) shows an example of a 3-layer TPM assembly generated by this additive construction method. The multiscale TPM combines a random tessellation for the "background PM" (i.e., the resulting thickest layer at the top) with ordered tessellations for the two thinner sub-layers at the bottom. Macroscopic features are added in Fig. 1(d) (highlighted in green) by direct manipulation of the matrix (image stack) in (c). Porous cracks were incorporated across the two thinner sub-layers by thickening the edges of a 2D Voronoi diagram (20 μm wide), followed by an extrusion in the TP direction. More realistic defect structures could be added by using more elaborated techniques or by direct combination of machine learning with tomography images [87,88].

2.2. Fluid network

As in PNM, the pore space is described using a geometrically representative pore-throat assembly inscribed in each polyhedral CV. Fig. 2(a)–(b) shows fluid networks inscribed in ordered and random CVs, along with the equivalent resistor network corresponding to an analysis of transport in j-direction. The fluid network is composed of a central pore body p, geometrically similar to the CV, and inlet/outlet truncated conical throats t arranged in parallel. Inlet and outlet faces of pore p and throat t are determined based on the outward unit normal vector to each face of a CV, $\bar{n}$, according to Eqs. (1a)–(1b)

$$\text{Inlet}: \quad \bar{n} \cdot \bar{e}_j < 0 \tag{1a}$$

$$\text{Outlet}: \quad \bar{n} \cdot \bar{e}_j > 0 \text{ (ordered)}, \quad \bar{e}_j \geq 0 \text{ (random)} \tag{1b}$$

where $\bar{e}_j$ is the unit vector in j-direction ($\bar{e}_x$, $\bar{e}_y$, $\bar{e}_z$). As in sealed permeameters, a face of an ordered CV where $\bar{n} \cdot \bar{e}_j = 0$, i.e., perfectly perpendicular to j-direction, is taken as a no-flux face [10,16,30]. For random CVs, CV faces are considered outlets by default if the rare but possible condition $\bar{n} \cdot \bar{e}_j = 0$ is met.

The central pore body p is scaled by a factor $\alpha_p < 1$ with respect to the CV, so that the points that define p and CV, $\bar{P}_p$ and $\bar{P}_{cv}$, are related according to Eq. (2)

$$\bar{P}_p = \bar{C}_{cv} + \alpha_p \left(\bar{P}_{cv} - \bar{C}_{cv} \right) \tag{2}$$

where $\bar{C}_{cv}$ is the position vector of the CV centroid.

The truncated conical throats are disposed in parallel, connecting every face of a CV, fcv, with the corresponding pore body face, fpb. The throat radii at every CV face, R_t^{fcv}, and pore body face, R_t^{fpb}, are given by Eqs. (3a)–(3b)

$$R_t^{\text{fcv}} = |\bar{\beta}_t \, \bar{n}| \, \alpha_t R_t^{\max} \tag{3a}$$

$$R_t^{\text{fpb}} = |\bar{\beta}_p \, \bar{n}| \, \alpha_p R_t^{\text{fcv}} \tag{3b}$$

where $\bar{\beta}_t$, α_t and $\bar{\beta}_p$, α_p are directional, isotropic scaling parameters relating $R_t^{\text{fcv}}/R_t^{\max}$ and $R_t^{\text{fpb}}/R_t^{\text{fcv}}$ ($\beta_i \leq 1$, $\alpha_i \leq 1$), respectively, $\bar{n}$ is the outward unit normal vector to fcv, and $R_t^{\max}$ is the radius of the maximum inscribed circle at fcv (determined by means of the Euclidean distance transform [89]).

Pore bodies and throats are uniquely defined in terms of transport by a reference transport area, $A_{t,p}^{\text{ref}}$, equivalent length, $L_{t,p}^{eq}$, and unit direction vector, $\bar{\ell}_{t,p}$. For pore body p, the transport properties in j-direction (x, y, z) can be directly scaled from those of the CV (see CV metrics in Section 4 below), according to Eqs. (4a)–(4c)

$$A_p^{jj} = \alpha_p^2 A_{cv}^{jj} \tag{4a}$$

$$L_p^{eq,j} = \alpha_p L_{cv}^j \tag{4b}$$

$$\bar{\ell}_p^j = \frac{A_{cv}^{ij}}{\|A_{cv}^{jj}\|} \tag{4c}$$

where A_{cv}^{ij} and L_{cv}^j are the projected CV area in i-direction and CV metric corresponding to transport in j-direction, respectively (A_{cv}^{jj} is equal to the projected CV area in j-direction). For throat t, the transport properties can be extracted from the geometry of truncated cones, according to Eqs. (4d)–(4f)

$$A_t^{\text{ref}} = A^{\text{fcv}} \tag{4d}$$

$$L_t^{eq} = \left\| \bar{P}_t^{\text{fcv}} - \bar{P}_t^{\text{fpb}} \right\| c_{tf} = L_t c_{tf} \tag{4e}$$

$$\bar{\ell}_t = \frac{\bar{P}_t^{\text{fcv}} - \bar{P}_t^{\text{fpb}}}{\left\| \bar{P}_t^{\text{fcv}} - \bar{P}_t^{\text{fpb}} \right\|} \tag{4f}$$

where A^{fcv} is the circular area of throat t at fcv, $\bar{P}_t^{\text{fcv}}$ and $\bar{P}_t^{\text{fpb}}$ are the position vectors of circle centers of throat t at fcv and fpb, respectively, and $c_{tf} \geq 1$ is the shape factor of throat t. The shape factor of conical throats with a linearly variable cross-section around the central axis ($\bar{P}_t^{\text{fcv}}, \bar{P}_t^{\text{fpb}}$) can be determined from the solution to the 1D scalar conservation equation along throat t (l-coordinate), as given by Eq. (5a)

$$\frac{\mathrm{d}}{\mathrm{d}l} \left[-A(l) \Pi_t \frac{\mathrm{d}\pi(l)}{\mathrm{d}l} \right] = 0 \Rightarrow -\frac{\mathrm{d}\pi(l)}{\mathrm{d}l} = \frac{j_{t,\ell}}{\Pi_t A(l)} \tag{5a}$$

where $\pi = C, p$ and $\Pi = D, K_t$ are the scalar and the property of interest (species concentration, C, and bulk diffusivity, D, vs. pressure, p, and throat permeability, K_t), and $j_{t,l}$ is the (constant) species flux rate across t. Imposing boundary conditions at the inlet/outlet of throat t, Eq. (5b) can be derived

$$\Delta \pi_t = j_{t,\ell} \int_0^{L_t} \frac{\mathrm{d}l}{\Pi_t(l) \, A_t(l)} \tag{5b}$$

The species flux rate referenced to the maximum throat area, $A_t^{\max}$, and internal property (in the case of permeability), $\Pi_t^{\max}$, can be expressed according to (5c)

$$A_t^{\max} \Pi_t^{\max} \frac{\Delta \pi_t}{L_t^{eq}} = \frac{\Delta \pi_t}{\int_0^{L_t} \frac{\mathrm{d}l}{\Pi_t(l) \, A_t(l)}} = j_{t,l} \tag{5c}$$

Therefore, L_t^{eq} is equal to the equivalent length for continuum resistors in series [9,90], as given by Eqs. (5d)–(5e)

$$\text{Diffussivity}: \quad L_t^{eq} = \int\limits_0^{L_t} \frac{A_t^{\max} \, \mathrm{d}l}{A_t(l)} \qquad \Rightarrow \frac{L_t^{eq}}{L_t} = \int\limits_0^1 \frac{\mathrm{d}\tilde{l}}{\tilde{A}_t(\tilde{l})} \qquad = c_{td} \tag{5d}$$

$$\text{Permeability}: \quad L_t^{eq} = \int\limits_0^{L_t} \frac{K_t^{\max} A_t^{\max} \, \mathrm{d}l}{K_t(l) \, A_t(l)} \Rightarrow \frac{L_t^{eq}}{L_t} = \int\limits_0^1 \frac{\mathrm{d}\tilde{l}}{\tilde{K}_t(\tilde{l}) \, \tilde{A}_t(\tilde{l})} = c_{th} \tag{5e}$$

with

$$\tilde{A}_t(\tilde{l}) = \tilde{A}_t^{\min} + (1 - \tilde{A}_t^{\min})\tilde{l}; \quad \tilde{K}_t(\tilde{l}) = \tilde{K}_t^{\min} + (1 - \tilde{K}_t^{\min})\tilde{l} \tag{5f}$$

where $\tilde{A}_t = A_t(l)/A_t^{\max}$ and $\tilde{K}_t = K_t(l)/K_t^{\max}$ are the normalized cross-section and permeability with respect to fcv ($\tilde{A}_t^{\min} = A_t^{\min}/A_t^{\mathrm{fcv}} \le 1$, $\tilde{K}_t^{\min} = K_t^{\min}/K_t^{\mathrm{fcv}} \le 1$), and the dimensionless coordinate along t is $\tilde{l} = l/L_t$. The shape factor c_t accounts for bottlenecks caused by a narrowing transport area ($c_t = 1$ for constant area, and $c_t \to \infty$ when $\tilde{A}_t^{\min} \to 0$). ($A_t^{\max}$, $K_t^{\max}$) and ($A_t^{\min}$, $K_t^{\min}$) are equal to the throat circular area, $A_t = \pi R_t^2$, and permeability, $K_t = R_t^2/8$, with $R_t = R_t^{\mathrm{fcv}}$ and $R_t = R_t^{\mathrm{fpb}}$ at the CV and the pore body faces, respectively. Integrals were computed using the *trapz* function. Pore volume can be directly determined from the CV volume by similarity

$$V_p = \alpha_p^3 V_{cv} \tag{6a}$$

where V_{cv} can be calculated with the *convexhulln* function. Throat volume can be determined analytically through the expression for a truncated cone of height L_t

$$V_t = \frac{1}{3}\pi L_t \left[(R_t^{\mathrm{fcv}})^2 + (R_t^{\mathrm{fpb}})^2 + R_t^{\mathrm{fcv}} R_t^{\mathrm{fpb}} \right] \tag{6b}$$

where L_t is the length of throat t. The average porosity can be easily modified using the scaling parameters α_i and $\bar{\beta}_i$.

2.3. Dual or complementary solid network

As shown in Fig. 2(a)–(b), the solid network inscribed in a CV is given by the complementary network to the fluid network (pore body conductivity is considered to be negligible). Unlike fluid throats, the shapeless form of solid throats is implicitly defined by the enclosed volume between a CV and the corresponding pore space. It is convenient to subdivide the solid space into N_t solid nodes or partitions, as imposed by the morphology of the fluid network. Each solid partition encompasses the volume enclosed between fcv and fpb minus the volume of the confined fluid throat t. Consequently, solid throats are independent elements arranged in parallel, which connect fcv with the faces that delimit a solid node, fsn. For an analysis of transport in j-direction, only area pairs ps preferentially oriented in that direction are taken into account. For example, face pairs with a projected unit direction vector in absolute value higher than th in j-direction ($|\bar{\ell}_{ps} \cdot \bar{e}_j| \ge th$) – $th = 0.7$ was considered here. Rather complex topologies with numerous solid connections arise when the number of CV faces is increased in random networks. For ordered parallelepipedal solid networks, there are 10 solid area pairs in each solid node, since a partition is bounded by 5 conductive faces (excluding fpb). Inlet and outlet solid throats are meaningless, since every solid pair connects an inlet with an outlet, and there is not a central "solid pore body".

The reference solid area, $A_{ps}^{\mathrm{ref},j}$, of a solid pair ps, corresponding to an analysis in j-direction, is determined by the maximum of the two connecting solid areas, according to Eq. (7a)

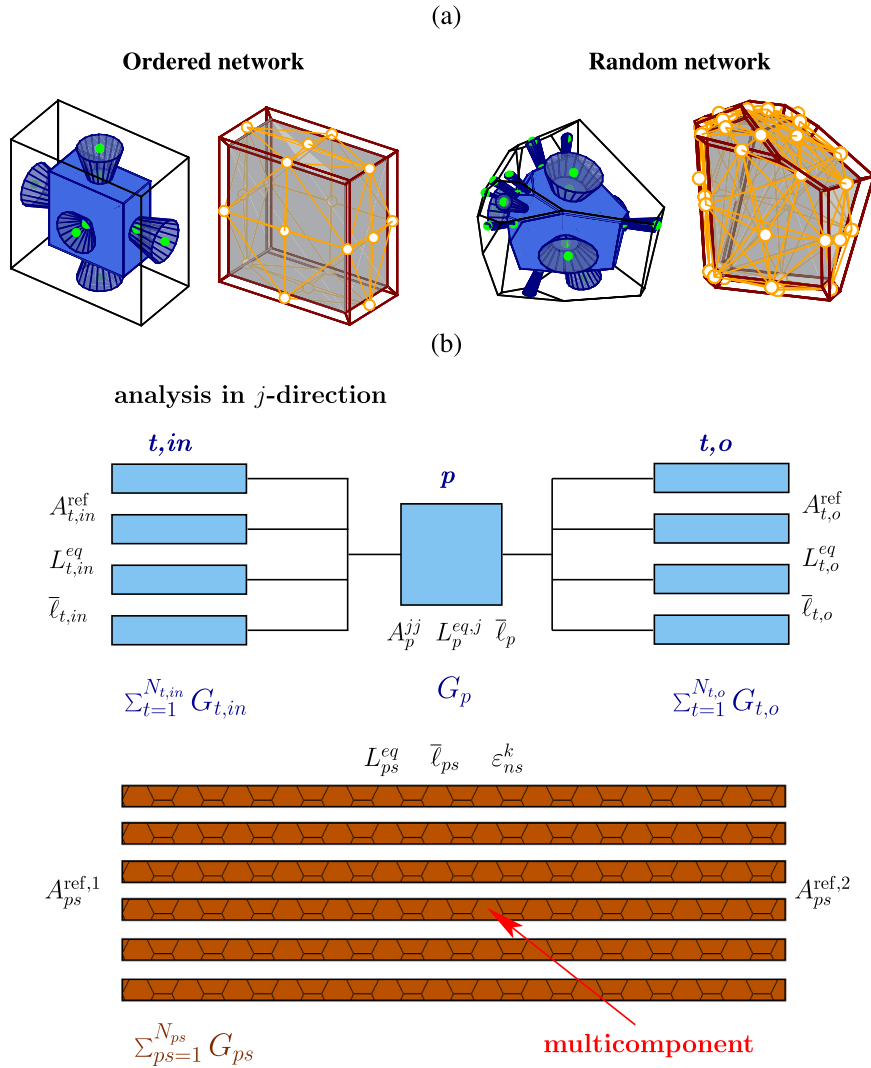$$A_{ps}^{\mathrm{ref},j} = \max\left(A_{ps}^{1,j}, A_{ps}^{2,j} \right) \tag{7a}$$

Similarly, the equivalent length, L_{ps}^{eq}, and unit direction vector, $\bar{\ell}_{ps}$, are obtained from the centroids of the two connecting solid areas, P_{ps}^1 and P_{ps}^2, as given by Eqs. (7b)–(7c)

$$L_{ps}^{eq} = \left\| \bar{P}_{ps}^1 - \bar{P}_{ps}^2 \right\| c_{ps} = L_{ps}^j c_{ps} \tag{7b}$$

$$\bar{\ell}_{ps} = \frac{| \bar{P}_{ps}^1 - \bar{P}_{ps}^2 |}{\left\| \bar{P}_{ps}^1 - \bar{P}_{ps}^2 \right\|} \tag{7c}$$

where c_{ps} is the shape factor of solid pair ps. Note that the absolute value makes results independent of the $\bar{\ell}_{ps}$ orientation, since solid pairs are treated as independent elements and the concept of inlet/outlet is meaningless in the solid network. Considering 1D continuum resistors in series [9,90], L_{ps}^{eq} of solid pair ps is given by Eq. (8a)

$$\frac{L_{ps}^{eq,j}}{L_{ps}^j} = \int\limits_0^1 \frac{\mathrm{d}\tilde{l}}{\tilde{A}_{ps}^j(\tilde{l})} = c_{ps}; \quad \tilde{A}_{ps}^j(\tilde{l}) = \tilde{A}_{ps}^{\min} + (1 - \tilde{A}_{ps}^{\min})\tilde{l} \tag{8a}$$

(a)

Ordered network   **Random network**

(b)

analysis in j-direction

Fig. 2. (a) Ordered and random polyhedral control volumes, showing the fluid network composed of a pore body p geometrically similar to the CV and truncated conical throats t, and the solid network around the central pore body. (b) Equivalent resistor network of the fluid and solid networks, corresponding to an analysis of transport in j-direction. Inlet and outlet fluid throats, t, in and t, o, are arranged in parallel between them and in series with the intermediate pore body p. Solid pairs ps connect solid inlet/outlet and are arranged in parallel between them. The reference transport area, A_i^{ref}, equivalent length, L_i^{eq}, and unit direction vector, $\overline{\ell}_i$, are indicated. The equivalent conductance of the resistors is denoted by G_i.

where $\tilde{A}_{ps}^j = A_{ps}^j / A_{ps}^{\mathrm{max},j}$ is the normalized area ratio with respect to the maximum area of face pair ps ($\tilde{A}_{ps}^{\min} = A_{ps}^{\min,j} / A_{ps}^{\max,j}$), and $\tilde{l} = l / L_{ps}^j$ is the normalized coordinate along solid pair ps. The area ratio of the porous solid phase can be estimated as $A / A_{\mathrm{bulk}} \simeq \varepsilon_{s,ps}^{2/3}$ based on the solid fraction in a solid node, ε_{ns}, so that Eq. (8b) is obtained

$$\frac{L_{ps}^{eq,j}}{L_{ps}^j} = \varepsilon_{ns}^{-2/3} \int_0^1 \frac{\mathrm{d}\tilde{l}}{\tilde{A}_{ps}^{\mathrm{bulk},j}(\tilde{l})} = c_{ps}; \quad \tilde{A}_{ps}^{\mathrm{bulk},j}(\tilde{l}) = \tilde{A}_{ps}^{\mathrm{bulk},\min} + (1 - \tilde{A}_{ps}^{\mathrm{bulk},\min})\tilde{l} \tag{8b}$$

where $A_{ps}^{\mathrm{bulk},j}$ is the bulk (i.e., fully solid area) of solid pair ps. The shape factor, $c_{ps} = L_{ps}^{eq,j}(L_{ps}^j)^{-1} \geq 1$, due to the constriction of the flux by the porous solid geometry. The solid fraction of a solid node ns, ε_{ns}, can be determined by subtracting the volume enclosed between fcv–fpb and the volume of the immersed throat, $V_{ns} = V_{scv} - V_t$. The volume of the sub CV between fcv–fpb, V_{scv}, is equal to that of a truncated prism of height L_t, as given by Eq. (9)

$$V_{scv} = \frac{1}{3} L_t \left(A^{\mathrm{fcv}} + A^{\mathrm{fpb}} + \sqrt{A^{\mathrm{fcv}} A^{\mathrm{fpb}}} \right) \tag{9}$$

This expression is simplified to Eq. (6b) for a truncated conical throat (circular cross-section).

For multi-component materials with N_k solid components distributed among N_t solid nodes, two conditions must be fulfilled to determine the volume fraction per unit solid volume of component k in solid node ns, ε_k^{ns}: (*i*) the sum of the volume fraction of all solid components in each solid node ns must be equal to one, and (*ii*) the sum of the volume fraction of solid component k over all solid nodes must be equal to a prescribed solid volume fraction per unit solid volume $\varepsilon_{k,s}$ in the corresponding CV (the prescribed total sum must be equal to one, $\sum_{k=1}^{N_k} \varepsilon_{k,s} = 1$)

$$\sum_{k=1}^{N_k} \varepsilon_{k,s}^{ns} = 1 \qquad \forall \text{ solid node } ns \tag{10a}$$

$$\sum_{ns=1}^{N_t} \varepsilon_{ns}\varepsilon_{k,s}^{ns} = \varepsilon_s\varepsilon_{k,s} \quad \forall \text{ solid component } k \tag{10b}$$

where ε_{ns} is the volume fraction of solid node ns per unit total volume, and ε_s is the solid volume fraction in the examined CV. The above two physical constraints lead to $N_k + N_t$ equations for $N_t \times N_k$ unknowns $\varepsilon_{k,s}^{ns}$. The solution to the constrained indeterminate system of equations (10a)-(10b) can be simplified by looking only for solutions that match condition (10a), since condition (10b) is statistically satisfied as the number of solid nodes is significantly high. If variables are random and independent (as it is usually the case), the expected value of condition (10b) yields Eq. (10c)

$$\mathrm{E}(\varepsilon_{ns}\varepsilon_{k,s}^{ns}) = \mathrm{E}(\varepsilon_{ns})\,\mathrm{E}(\varepsilon_{k,s}^{ns}) = \varepsilon_s\varepsilon_{k,s} \tag{10c}$$

The normalization of ε_k^{ns} can be easily accomplished by prescribing random values from prescribed distributions (e.g., random distributions between minimum and maximum thresholds) and normalizing each volume fraction by the total sum to ensure that $\sum_{k=1}^{N_k} \varepsilon_{k,s}^{ns} = 1$ is matched. Tests with a common number of solid nodes, $N_{ns} \approx 8 - 15$, showed that the error incurred in meeting condition (10b) is typically lower than 5%, which is a reasonable approximation. It is also worth noting that there is not any limitation to keep $\varepsilon_{k,s}$ constant. It can vary according to a predefined spatial distribution (e.g., random and patterned distributions found in untreated and engineered TPM [91,92]).

3. Local microstructural properties

Many microstructural properties can be locally extracted on a CV basis using the geometrical information from the fluid and solid networks. Effective transport properties can be locally correlated as a function of microstructural properties, as a complementary procedure to the tensorization method presented in Section 4. The use of correlations is necessary for modeling TPM assemblies with large separation of scales between layers (e.g., GDL+MPL+CL in a PEMFC), since the computational cost of including pore sizes that span around three orders of magnitude can be prohibitive. In multiscale TPM, it is convenient to generate virtual CVs in which there are N_p pores in each CV with a pore size distribution downscaled by a multiscale factor S_p with respect to the pore size distribution used for CV generation ($R_p = R_p^{\mathrm{gen}}/S_p$). For example, in the simulations conducted for the cracked MPL+GDL presented in Section 6, the MPL was modeled with $N_p = 2.5 \times 10^4$ and $S_p = 18$ using CVs with a size around 5 times lower than that used for the GDL. The resulting porosity was $\varepsilon \approx 0.45$ and the average pore size was $R_f \approx 100$ nm. Dry effective diffusivity was correlated as a function of local porosity by a power-law function.

Below, expressions for the volume fraction, ε_i, length, L_i, anisotropy ratio, AR_i, size, R_i, and specific surface area, a_i, are presented for the fluid phase and single/multi-component solid phase. In addition, common expressions for entry capillary pressure and (static) contact angle, p_e and θ, are presented. Local properties determined on a CV basis (ε_i, L_i, AR_i, R_i and a_i) can be exported to 3D image stacks similar to other CV variables, such as TPM regions, Voronoi cells and effective properties (see Fig. 1). However, local variables corresponding to CV-CV interfaces (p_e) must be exported to a CFD solver using an adjacency matrix between CV identifiers (e.g., binary ASCII file). Properties modeled with the scaling argument commented above for the number of pores and pore size are presented at the end. Average properties in larger TPM regions could be simply determined by volume averaging local properties determined on a CV basis.

3.1. Volume fraction

The volume fractions of the fluid phase (porosity) and the solid phase, ε and ε_s, respectively, along with the volume fraction of solid component k per unit total volume, ε_k, in multi-component TPM, are given by Eq. (11)

$$\varepsilon = \frac{V_f}{V_{cv}} = \frac{V_p + \sum_{t=1}^{N_t} V_t}{V_{cv}}; \quad \varepsilon_s = 1 - \varepsilon; \quad \varepsilon_k = \varepsilon_{k,s}\varepsilon_s \tag{11}$$

where V_{cv} is the volume of a control volume (determined by the *convexhulln* function), and V_f, V_p and V_t are the volumes of the fluid phase, pore p and throat t in that CV, respectively (all of them determined either by similarity or analytically, see Eqs. (6a) and (6b)), and $\varepsilon_{k,s}$ is the prescribed local volume fraction of solid component k in the CV.

3.2. Length and anisotropy ratio

The mean geometrical length of the fluid and solid phases, L_f and L_s, can be quantified by the volume average length of fluid throats and solid pairs (in all j-directions), L_t and L_{ps}^j, and the diametrical pore length, according to Eq. (12a)

$$L_f = \frac{\sum_{t=1}^{N_t} L_t V_t + 2\left(\frac{3V_p}{4\pi}\right)^{1/3} V_p}{\varepsilon V_{cv}}; \quad L_s = \sum_{j=1}^{3} \frac{\sum_{ps=1}^{N_{ps}^j} L_{ps}^j \varepsilon_{ns}}{3\varepsilon_s} \tag{12a}$$

where $\varepsilon_{ns} = (V_{scv} - V_t)/V_{cv}$ is expressed per unit CV volume (see Eqs. (6b) and (9)).

TPM usually feature significantly different properties in the IP direction compared to the TP direction due to the use of pseudo-2D manufacturing techniques [1,93]. The anisotropy ratios between the mean length in the material plane (x, z-direction) and the through-plane direction (y-direction), AR_f and AR_s, can be determined according to Eq. (12b)

$$\mathrm{AR}_f = \frac{\sum_{t=1}^{N_t} L_t^{ip} V_t + L_p^{ip} V_p}{\sum_{t=1}^{N_t} L_t^{tp} V_t + L_p^{tp} V_p}; \quad \mathrm{AR}_s = \sum_{j=1}^{3} \frac{\sum_{t=1}^{N_{ps}^j} L_{ps}^{ip} \varepsilon_{ns}}{3\sum_{t=1}^{N_{ps}^j} L_{ps}^{tp} \varepsilon_{ns}} \tag{12b}$$

where the average directional lengths of fluid throat t, pore p and solid pair ps are given by Eqs. (12c)–(12e)

$$L_t^{ip} = \frac{L_t^x + L_t^z}{2}; \qquad L_t^{tp} = L_t^y \tag{12c}$$

$$L_p^{ip} = \frac{\alpha_p(L_{cv}^{xx} + L_{cv}^{zz})}{2}; \quad L_p^{tp} = \alpha_p L_{cv}^{yy} \tag{12d}$$

$$L_{ps}^{ip} = \frac{L_{ps}^x + L_{ps}^z}{2}; \qquad L_{ps}^{tp} = L_{ps}^{yy} \tag{12e}$$

In this expression, α_p is the pore scaling parameter, and L_{cv} is the CV metric (introduced in Section 4).

3.3. Size

The mean size (i.e., radius) of the fluid and solid phases, R_f and R_s, and the radius of solid component k, R_k, in multi-component materials, can be determined according to Eq. (13)

$$R_f = \frac{\sum_{t=1}^{N_t} R_t^{\mathrm{avg}} V_t + \left(\frac{3V_p}{4\pi}\right)^{1/3} V_p}{\varepsilon V_{cv}}; \quad R_s = \left(\frac{\varepsilon_s V_{cv}}{\pi L_s}\right)^{1/2}; \quad \frac{R_k}{R_s} = \left(\frac{\varepsilon_k}{\varepsilon_s}\right)^{1/2} \leq 1 \tag{13}$$

where R_t^{avg} is the mean radius of throat t, $R_t^{\mathrm{avg}} = (R_t^{\mathrm{fcv}} + R_t^{\mathrm{fpb}})/2$, L_s is the mean solid length given by Eq. (12a), and ε_k is the volume fraction of solid component k given by Eq. (11). The geometrical radii of the solid phase and the solid component k scale with the volume fraction ($R_i \to 0$ when $\varepsilon_i \to 0$).

3.4. Specific surface area

The specific surface area, a, plays a key role in reactive TPM (e.g., macroporous electrodes in redox flow batteries (RFBs) [13] and CLs in PEMFCs [14]). a is given by the fluid-solid interfacial area per unit total volume according to Eq. (14a)

$$a = \frac{\sum_{t=1}^{N_t} A_t^{\mathrm{int}} + A_p^{\mathrm{int}}}{V_{cv}} \tag{14a}$$

where the fluid-solid interfacial areas of throat t and pore p are equal to Eqs. (14b)–(14c)

$$A_t^{\mathrm{int}} = \pi s(R^{\mathrm{fcv}} + R^{\mathrm{fpb}}); \quad s = \sqrt{(R^{\mathrm{fcv}} - R^{\mathrm{fpb}})^2 + L_t^2} \tag{14b}$$

$$A_p^{\mathrm{int}} = \alpha_p^2 A_{cv}^{\mathrm{int}} - \pi(R^{\mathrm{fpb}})^2 \tag{14c}$$

Here, s is the apothem of the truncated conical throat t. The interfacial area of a CV was determined by Delaunay triangulation using the 2D *delaunay* function on each fcv face.

3.5. Entry capillary pressure and contact angle

The entry capillary pressure of a fluid throat, $p_{e,t}$, is determined by the radius and internal contact angle, θ_t. $p_{e,t}$ is usually estimated using Washburn's equation for a cylindrical pore [94], as given by Eq. (15a)

$$p_{e,t} = -\frac{2\sigma}{R_t^{\text{avg}}}\cos\theta_t \tag{15a}$$

where σ is the surface tension of the working fluid pair in the TPM, $R_t^{\text{avg}} = (R_t^{\text{fcv}} + R_t^{\text{fpb}})/2$ is the average throat radius, and θ_t is the contact angle in throat t.

For fibrous TPM, such as carbon paper, felt and cloth, the convergent/divergent geometry of pore space is better described by a toroidal pore model (Purcell's equation). The entry capillary pressure of a throat takes the form of Eq. (15b) (modified Washburn equation) [16,30,89,94]

$$p_{e,t} = -\frac{2\sigma}{R_t^{\text{avg}}}\frac{\cos(\theta_t - \gamma)}{1 + \dfrac{d_s}{2R_t^{\text{avg}}}(1 - \cos\gamma)}; \quad \gamma = \theta - \pi + \arcsin\left(\frac{\sin\theta_t}{1 + \dfrac{2R_t^{\text{avg}}}{d_s}}\right) \tag{15b}$$

where d_s is the characteristic fiber diameter.

In practice, the volume average entry capillary pressure inside a CV was used for two-phase calculations. This simplification could be omitted but is convenient to reduce the amount of data during calculation of the global adjacency matrix, so that a CV is identified by only one p_e value (a reasonable approximation for many applications). Volume averaged p_e in a CV and $p_{e,t}$ are related by Eq. (15c)

$$p_e = \frac{\sum V_t p_{e,t}}{\sum V_t} \tag{15c}$$

where V_t is the volume of fluid throat t (Eq. (6b)).

A representative constant contact angle ($\theta_t = \text{const.}$) can be estimated based on the solid-fluid-gas system under analysis [89,94,95]. For multi-component materials (e.g., polytetrafluoroethylene (PTFE)-treated GDLs), wettability can be made dependent on the solid composition (local PTFE content) using semi or fully empirical correlations. For example, the contact angle of carbon paper has been reported to increase with PTFE content by weight [96]. In addition, distributions of PTFE content and internal contact angle can be extracted by combining X-CT and image processing [97,98]. This information can be readily incorporated into the CV generation process to analyze the effect of spatially-varying solid composition, either in conventional or engineered TPM [95,99,100].

Many other formulations have been reported for $p_{e,t}$ and θ_t depending on the pore shape (triangular, squared, rectangular, hyperbolic, etc.), roughness, and multiphase system under analysis (see, e.g., [53,101,102] among others).

In multiscale porous assemblies, where the pore radius of fine TPM is downscaled by a factor S_p, $R_f = R_p = R_t$, assuming no internal redistribution of average pore size inside each CV. Other microstructural properties of interest (e.g., volume fraction, length and specific surface area) can be determined based on a spherical pore geometry, according to the number of pores in each CV, N_p, and the actual downscaled pore radius (see Eq. (16))

$$\varepsilon = \min\left(N_p\frac{4\pi R_p^3}{3V_{cv}}, \varepsilon^{\text{max}}\right); \quad \varepsilon_s = 1 - \varepsilon; \quad L_f = 2R_p; \quad L_s = (\varepsilon_s V_{cv})^{1/3}; \quad a = N_p\frac{4\pi R_p^2}{V_{cv}} \tag{16}$$

where ε^{max} is the maximum allowed local porosity ($\varepsilon^{\text{max}} \simeq 0.95$), and V_{cv} is the CV volume.

4. Local effective transport properties: tensorization

In this section, a tensorization method for extracting local effective transport property tensors (higher order mathematical element) from a resistor network (lower order mathematical element) is presented. The analysis for the fluid network considers a fully 3D description of space (effective diffusivity and permeability), while the methodology for the more complex solid network relies on a simplified 1D description to determine 3D tensors (solid-phase conductivity, such as electrical or thermal conductivity). In all cases, the approach is valid for transport of a scalar π (e.g., species concentration) governed by a Laplace-like equation of the form of Eq. (17a)

$$\nabla \cdot \bar{J} = 0; \quad \bar{J} = -\Pi\nabla\pi \tag{17a}$$

where $\bar{J}$ is the scalar flux (e.g., species diffusive flux), and Π is the scalar diffusivity (e.g., species mass diffusivity). When Π is non-linear, $\Pi(\pi)$, Eq. (17a) can be linearized by means of Kirchhoff's transformation [103–105], as given by Eq. (17b)

$$\nabla\Theta = \Pi(\pi)\nabla\pi \rightarrow \Theta(\pi) = \int_0^\pi \Pi(\eta)\,d\eta, \tag{17b}$$

so it is reduced to a linear Laplace equation with unity diffusivity in terms of the potential Θ (see Eq. (17c))

$$\nabla^2\Theta = 0 \tag{17c}$$

The inverse Kirchhoff's transformation can be used in CFD calculations to determine π^{cfd} from the computed value Θ^{cfd}, according to Eq. (17d)

$$\Theta^{\mathrm{cfd}} - F(\pi^{\mathrm{cfd}}) = 0 \to \pi^{\mathrm{cfd}}(\Theta^{\mathrm{cfd}}); \quad F(\pi^{\mathrm{cfd}}) = \int\limits_{0}^{\pi^{\mathrm{cfd}}} \Pi(\eta)\,\mathrm{d}\eta \tag{17d}$$

This equation can be solved analytically or numerically [106].

4.1. Effective diffusivity tensor

According to Fick's law, the effective diffusivity tensor relates the average diffusive flux in i-direction through a porous CV, j_i, when a macroscopic concentration difference is prescribed in j-direction, ΔC_j. In index notation, D_{ij}^{eff} takes the form of Eq. (18)

$$D_{ij}^{\mathrm{eff}} = \frac{\frac{1}{V_{cv}}\int_{V_{cv}} j_i\,\mathrm{d}V}{\frac{\Delta C_j}{L_{cv}}} = \frac{L_{cv}\int_{V_f} j_i\,\mathrm{d}V}{V_{cv}\,\Delta C_j} \tag{18}$$

where V_{cv} and V_f are the total and fluid volumes of the porous CV, respectively. No flux holds in solid regions.

The CV length, L_{cv}, is usually unknown except for ordered CVs with a fully padded geometry aligned to x, y, z-direction (e.g., a parallelepipedal CV). However, this is an infrequent case for polyhedral CVs. As shown in Fig. 3(a), the reference length of a CV is in general a diagonal metric, L_{cv}^{jj}, obtained from the condition that the effective diffusivity equals the bulk diffusivity when no blocking (i.e., no resistor network) is present in a CV – the CV is simply a bulk, isotropic medium of diffusivity D. In other words, the CV tessellation and inlet/outlet distribution alter ordinary space by themselves. Introducing this condition, Eq. (18) leads to Eq. (19)

$$\frac{D_{jj}^{\mathrm{eff}}}{D} = -\frac{L_{cv}^{jj}\int_{V_{cv}} \nabla C|_j\,\mathrm{d}V}{V_{cv}\,\Delta C_j} = 1 \Rightarrow L_{cv}^{jj} = \frac{V_{cv}\,\Delta C_j}{\int_{V_{cv}} - \nabla C|_j\,\mathrm{d}V} \tag{19}$$

where $\nabla C|_j$ is the j-component of the concentration gradient when ΔC_j is imposed in j-direction. The volume integral can be transformed into a surface integral by means of the gradient theorem (reduced form of the divergence theorem [107]), so that Eq. (20) is obtained

$$\int\limits_{V_{cv}} -\nabla C\,\mathrm{d}V = \int\limits_{\Sigma_{in,o}} -C\overline{n}\,\mathrm{d}\sigma = -C_{in}\sum_{in} A_{in}^{\mathrm{fcv}}\overline{n}_{in} - C_o\sum_o A_o^{\mathrm{fcv}}\overline{n}_o \tag{20}$$

where C_{in} and C_o are the (virtually) prescribed inlet and outlet concentrations in j-direction, and $A_{in}^{\mathrm{fcv}}/A_o^{\mathrm{fcv}}$ and $\overline{n}_{in}/\overline{n}_o$ are the areas and outward unit normal vectors of inlet and outlet CV faces, respectively. The evaluation of the (unknown) concentration at walls is avoided, since the entire CV surface is decomposed into inlet and outlets. For ordered parallelepipedal CVs, the contribution of symmetric CV faces where $\overline{n}\cdot\overline{e}_j = 0$ cancels out due to the opposite sign of $\overline{n}$.
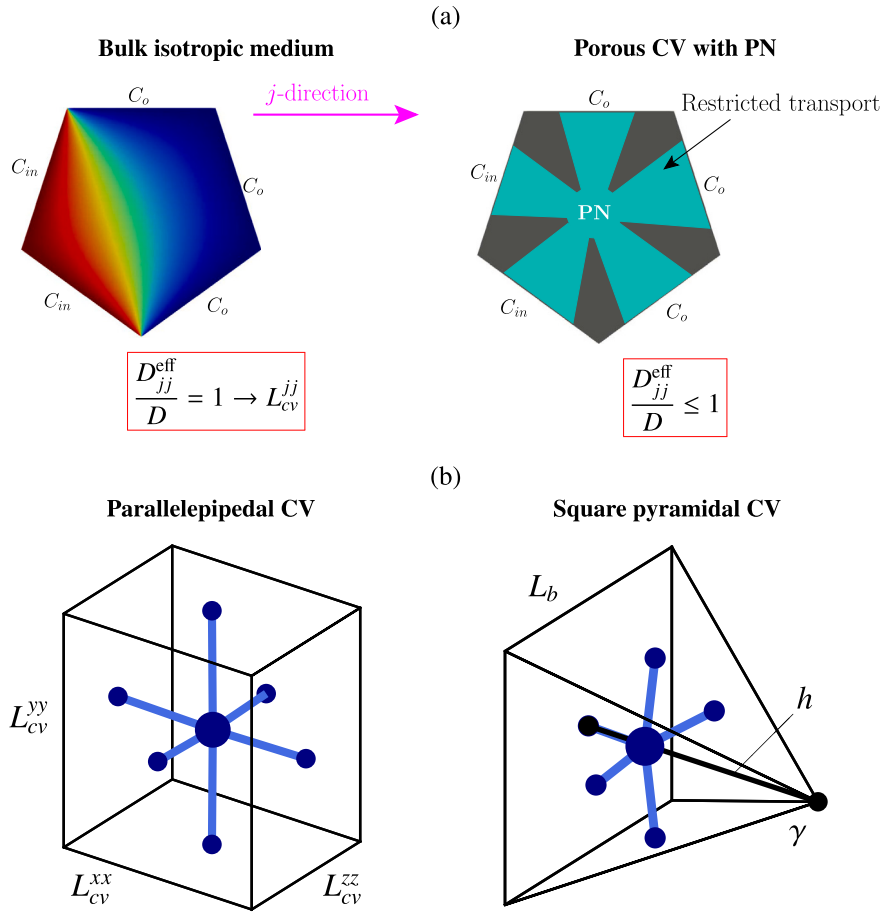
As shown in Fig. 3(a), faces in a CV are considered outlets by default, that is, C_o is taken as the nominal concentration. Hence, undefined faces of random polyhedral CVs where $\overline{n}\cdot\overline{e}_j = 0$, such as the upper horizontal face of the pentagon in Fig. (3), are treated as outlets. Inlets are identified according to the criterion (1a). The surface integral (20) can be re-written in terms of "gauge" concentrations $(C_{in} - C_o)$ using the principle of linear superposition (21a) [108,109]

$$\int\limits_{\Sigma_{in,o}} -C\overline{n}\,\mathrm{d}\sigma = -\int\limits_{\Sigma_{in}} C_{in}\overline{n}\,\mathrm{d}\sigma - \int\limits_{\Sigma_o} C_o\overline{n}\,\mathrm{d}\sigma =$$

$$-\int\limits_{\Sigma_{in}} C_{in}\overline{n}\,\mathrm{d}\sigma - \overset{0}{\cancel{\oint\limits_{\Sigma_{cv}} C_o\overline{n}\,\mathrm{d}\sigma}} + \int\limits_{\Sigma_{in}} C_o\overline{n}\,\mathrm{d}\sigma = -\int\limits_{\Sigma_{in}} (C_{in} - C_o)\overline{n}\,\mathrm{d}\sigma = -(C_{in} - C_o)\sum_{in} A_{in}^{\mathrm{fcv}}\overline{n}_{in} \tag{21a}$$

or (21b)

$$\int\limits_{\Sigma_{in,o}} -C\overline{n}\,\mathrm{d}\sigma = -\int\limits_{\Sigma_{in}} C_{in}\overline{n}\,\mathrm{d}\sigma - \int\limits_{\Sigma_o} C_o\overline{n}\,\mathrm{d}\sigma =$$

$$-\overset{0}{\cancel{\oint\limits_{\Sigma_{cv}} C_{in}\overline{n}\,\mathrm{d}\sigma}} - \int\limits_{\Sigma_o} C_o\overline{n}\,\mathrm{d}\sigma + \int\limits_{\Sigma_o} C_{in}\overline{n}\,\mathrm{d}\sigma = (C_{in} - C_o)\sum_o A_o^{\mathrm{fcv}}\overline{n}_o \tag{21b}$$

Here, it has been taken into account that the surface integral of a constant scalar over a closed surface is null due to self-cancellation of $\overline{n}$. The term $-\sum_{in} A_{in}^{\mathrm{fcv}}\overline{n}_{in} = \sum_o A_o^{\mathrm{fcv}}\overline{n}_o = \overline{A}_{cv}^j$ is equal to the projected cross-section of the convex hull to i-direction ($i = x, y, z$) for ΔC_j. A_{cv}^{ij} denotes the full tensor of CV projected areas including all i-directions (rows) and j-directions (columns). Incorporating (21a)-(21b) into (19), we yield Eq. (22)

(a)

Bulk isotropic medium

C_o

j-direction

C_{in}

C_o

C_{in}

C_o

$$\frac{D_{jj}^{\text{eff}}}{D} = 1 \rightarrow L_{cv}^{jj}$$

Porous CV with PN

C_o

Restricted transport

C_{in}

C_o

PN

C_{in}

C_o

$$\frac{D_{jj}^{\text{eff}}}{D} \leq 1$$

(b)

Parallelepipedal CV

L_{cv}^{yy}

L_{cv}^{xx}

L_{cv}^{zz}

Square pyramidal CV

L_b

h

γ

Fig. 3. (a) Schematic of the methodology used to determine the normalized effective diffusivity tensor, D_{ij}^{eff}/D, of a fluid network inscribed in a polyhedral CV. The physical constraint $D_{ij}^{\text{eff}}/D = 1$ is imposed on the bulk, isotropic medium to determine the tensor metric L_{cv}^{jj}, and $D_{ij}^{\text{eff}}/D < 1$ is then determined on the porous CV by volume averaging of the discretized pore network. Similar considerations apply for other effective transport properties. (b) Skeletonized representation of a fluid network inscribed in a parallelepipedal CV, defined by the side length, $(L_{cv,x}, L_{cv,y}, L_{cv,z})$, and a square pyramidal CV, defined by the base length, L_{cv}, and the height, h.

$$L_{cv}^{jj} = \frac{V_{cv}}{-\sum_{in} A_{in}^{\text{fcv}} \bar{n}_{in}^j} = \frac{V_{cv}}{\sum_{o} A_o^{\text{fcv}} \bar{n}_o^j} = \frac{V_{cv}}{A_{cv}^{jj}} \tag{22}$$

where $\bar{n}_{in}^j$ and $\bar{n}_o^j$ are the j-component of the outward unit normal vector of the inlet and outlet CV faces, respectively. L_{cv}^{jj} depends exclusively on CV geometrical properties, and can be interpreted as the 3D analog of the expression for 1D continuum resistors in series (Eq. (5d)) [9,90]. For a CV composed of a single throat, when j-direction points along the throat axis, $L_{cv}^{jj} = V_{cv}/A_t^{\max}$, since the solution holds axial symmetry, i.e., there is no net vector flux in any direction other than the axial direction. Hence, the normalized effective diffusivity, Eq. (19), takes the form of Eq. (23a)

$$\frac{D^{\text{eff}}}{D} = \frac{\int_{V_{cv}} -\nabla C|_j \, dV}{A_t^{\max} \Delta C_j} \tag{23a}$$

Introducing the result derived before in Eq. (5c), we yield Eq. (23b)

$$-\nabla C|_j = \frac{j_{t,\ell}}{DA(l)}; \quad j_{t,\ell} = \frac{\Delta C_j}{\int_0^{L_t} \frac{dl}{DA_t(l)}}, \tag{23b}$$

It can be verified the connection between the tensorization method and the expression for 1D continuum resistors in series through Eq. (23c)

$$\frac{D^{\text{eff}}}{D} = \left[\int_0^1 \frac{d\tilde{l}}{\tilde{A}_t(l)} \right]^{-1} \equiv \frac{L_t}{L_t^{eq}} \tag{23c}$$

All length metrics tend to infinity when $A_t^{\max} \to 0$.

Two simplified 3D examples for the CV metric are shown in Fig. 3(b): (left) a structured parallelepipedal CV, and (right) a square pyramidal CV. In the case of the parallelepiped, the application of Eq. (22) is straightforward

$$
L_{cv}^{jj} = \begin{matrix} i = x \\ i = y \\ i = z \end{matrix} \ V_{cv} \begin{bmatrix} \dfrac{1}{A_{cv}^{xx}} & 0 & 0 \\ 0 & \dfrac{1}{A_{cv}^{yy}} & 0 \\ 0 & 0 & \dfrac{1}{A_{cv}^{zz}} \end{bmatrix} = \begin{bmatrix} L_{cv}^{xx} & 0 & 0 \\ 0 & L_{cv}^{yy} & 0 \\ 0 & 0 & L_{cv}^{zz} \end{bmatrix}
\tag{24}
$$
$$
j = x \quad j = y \quad j = z
$$

where A_{cv}^{jj} and L_{cv}^{jj} are the projected cross-section and metric of the CV for $j = x, y, z$.

For the squared pyramid, the CV volume and the base and lateral areas, A_b and A_l, can be expressed in terms of the size of the base, L_b, and the pyramid height, h, leading to a diagonal CV metric with different expressions in x, y, z (see Eq. (25))

$$
V_{cv} = \frac{L_b^2 h}{3}; \quad A_b = L_b^2; \quad A_l = \frac{L_b}{4}\sqrt{4h^2 + L_b^2}
\tag{25}
$$

The projected area in the first column (ΔC_j imposed in axial x-direction) is simply given by the base of the square pyramid ($A_{cv}^{xx} = A_b$). In the transverse y, z-directions, $A_{cv}^{yy} = A_{cv}^{zz} = A_l \sin\gamma$, where $\sin\gamma = 2h/\sqrt{4h^2 + L_b^2}$, with γ the apex semi-angle. Consequently, (22) leads to the CV metric (26)

$$
L_{cv}^{jj} = \begin{bmatrix} \dfrac{h}{3} & 0 & 0 \\ 0 & \dfrac{2L_b}{3} & 0 \\ 0 & 0 & \dfrac{2L_b}{3} \end{bmatrix}
\tag{26}
$$

The metric is proportional to the reference geometrical length of the pyramid in x, y, z (h in the axial x-direction and L_b in the transverse y, z-directions). The proportionality factor decreases with the fluid space available for transport in a given direction, so it is lower in the axial direction compared to the transverse direction (1/3 vs. 2/3). Note that the inlets and the outlets are uniquely defined by their outward unit normal vectors $\bar{n}$ ($\bar{n} \cdot \bar{e}_j < 0$ for inlets and $\bar{n} \cdot \bar{e}_j \geq 0$ for outlets), so that the projected area for $j = x$ is always equal to A_b (positive value) regardless of the x-axis orientation. The same holds for other directions. The incorporation of the fluid network is accomplished by discretizing the volume integral in (18) according to the pore-throat geometry. For N_t (inlet+outlet) fluid throats t and one central pore body p, we yield Eq. (27a)

$$
D_{ij}^{\text{eff}} = \frac{L_{cv}^{jj}}{V_{cv}\Delta C_j}\left(\sum_{t=1}^{N_t} j_{t,i}V_t + j_{p,i}V_p\right); \quad j_{t,i} = D\frac{\Delta C_t}{L_t^{eq}}\ell_{t,i}; \quad j_{p,i} = D\frac{\Delta C_p}{L_p^{eq}}\ell_{p,i}
\tag{27a}
$$

where V_t, V_p is the t, p volume, $\ell_{t,i}, \ell_{p,i}$ is the i-component of the t, p unit direction vector pointing from higher to lower concentrations, L_t^{eq}, L_p^{eq} is the equivalent t, p length, and $\Delta C_t, \Delta C_p$ is the t, p concentration difference. Eq. (27a) can be re-written as Eq. (27b)

$$
D_{ij}^{\text{eff}} = \sum_{t=1}^{N_t} D_{t,ij}^{\text{eff}} + D_{p,ij}^{\text{eff}}; \quad D_{t,ij}^{\text{eff}} = \frac{\varepsilon_t}{\tau_{td}^{ij}}; \quad D_{p,ij}^{\text{eff}} = \frac{\varepsilon_p}{\tau_{pd}^{ij}}
\tag{27b}
$$

where $\varepsilon_t = V_t/V_{cv}$ and $\varepsilon_p = V_p/V_{cv}$ are the contributions of t and p to the total porosity, and τ_{td}^{ij} and τ_{pd}^{ij} are the (apparent) diffusive tortuosities of t and p between directions $i - j$ (see Eq. (27c))

$$
\tau_{td}^{ij} = \frac{\Delta C_j}{\Delta C_t}\frac{1}{\ell_{t,i}}\frac{L_t^{eq}}{L_{cv}^{jj}}; \quad \tau_{pd}^{ij} = \frac{\Delta C_j}{\Delta C_p}\frac{1}{\ell_{p,i}}\frac{L_p^{eq}}{L_{cv}^{jj}}
\tag{27c}
$$

The concentration differences, ΔC_t and ΔC_p, can be determined using the equivalent resistor networks presented in Fig. 2, neglecting edge and t-p-t connectivity effects in a first approximation. Alternatively, they can also be obtained from DNS, molecular dynamics simulations, experiments or even machine learning (see, e.g., the recent works [110–113]).

The effective tortuosity tensor, τ_d^{ij}, encompass the aggregated contribution of t and p, τ_{td}^{ij} and τ_{pd}^{ij}, as given by Eq. (27d) [41,42]

$$
\frac{D_{ij}^{\text{eff}}}{D} = \sum_{t=1}^{N_t} \frac{\varepsilon_t}{\tau_{td}^{ij}} + \frac{\varepsilon_p}{\tau_{pd}^{ij}} = \frac{\varepsilon}{\tau_d^{ij}} \Rightarrow \tau_d^{ij} = \varepsilon\left(\sum_{t=1}^{N_t}\frac{\varepsilon_t}{\tau_{td}^{ij}} + \frac{\varepsilon_p}{\tau_{pd}^{ij}}\right)^{-1} = \left[\sum_{t=1}^{N_t}\frac{(\varepsilon_t/\varepsilon)}{\tau_{td}^{ij}} + \frac{(\varepsilon_p/\varepsilon)}{\tau_{tp}^{ij}}\right]^{-1}
\tag{27d}
$$

The extended form of (27d) takes the form (27e)

$$\tau_d^{ij} = \left[\sum_{t=1}^{N_t} \frac{\Delta C_t}{\Delta C_j}\left(\frac{\varepsilon_t}{\varepsilon}\frac{L_{cv}^{jj}}{L_t^{eq}}\ell_{t,i}\right) + \frac{\Delta C_p}{\Delta C_j}\left(\frac{\varepsilon_p}{\varepsilon}\frac{1}{\alpha_p}\frac{A_{cv}^{ij}}{\|\bar{A}^j\|}\right)\right]^{-1} \equiv \left[\chi_{td,in}^j \Gamma_{t,in}^{ij} + \chi_{td,o}^j \Gamma_{t,o}^{ij} + \chi_{pd}^j \Gamma_p^{ij}\right]^{-1} \geq 1 \tag{27e}$$

where $\|\bar{A}^j\|$ is the magnitude of the CV projected area for ΔC_j.

The terms $\chi_{d,m}^j$ are the concentration partition coefficients, $\chi_{d,m}^j = \Delta C_m/\Delta C_j$, across inlet throats ($m = t, in$), pore ($m = p$) and outlet throats ($m = t, o$), whose sum is equal to one (neglecting any interfacial resistance, see below). $\chi_{d,m}^j$ is determined from mass conservation across the diffusive resistor network according to Eq. (28a)

$$\Delta C_{t,in}\sum_{t=1}^{N_{t,in}} G_{td,in}^j = \Delta C_{t,o}\sum_{t=1}^{N_{t,o}} G_{td,o}^j; \quad \Delta C_{t,in}\sum_{t=1}^{N_{t,in}} G_{td,in}^j = \Delta C_p G_{pd}^j \tag{28a}$$

where the diffusive conductances are given by Eq. (28b)

$$G_{td,in}^j = \frac{DA_{t,in}^{\text{ref}}}{L_{t,in}^{eq}}; \quad G_{td,o}^j = \frac{DA_{t,o}^{\text{ref}}}{L_{t,o}^{eq}}; \quad G_{pd}^j = \frac{DA_p^{jj}}{L_p^{jj}} = D\alpha_p\frac{A_{cv}^{jj}}{L_{cv}^{jj}} \tag{28b}$$

From (28a)-(28b), we yield Eq. (28c) for the partition coefficients $\chi_{d,m}^j$ ($m = t, in; t, o; p$)

$$\chi_{td,in}^j = \left[1 + \frac{G_{td,in}^j}{G_{td,o}^j} + \frac{G_{td,in}^j}{G_{pd}^j}\right]^{-1}; \quad \chi_{td,o}^j = \left[1 + \frac{G_{td,o}^j}{G_{td,in}^j} + \frac{G_{td,o}^j}{G_{pd}^j}\right]^{-1}; \quad \chi_{pd}^j = 1 - \chi_{td,in}^j - \chi_{td,o}^j \tag{28c}$$

A distributed interfacial conductance (i.e., resistance), $G_{d,\text{int}}^j$, can also be incorporated, resulting in an additional term $G_{td}^j/G_{d,\text{int}}^j$ in the summations of (28c). For $G_{d,\text{int}}^j \ll G_{td}^j$, the partition coefficients of t and p would vanish due to the dominant role of $G_{d,\text{int}}^j$, severely reducing the network diffusivity.

Considering that the volume of a truncated conical throat is given by Eq. (29a)

$$V_t = L_t\int_0^1 A_t(\tilde{l})\,d\tilde{l} \tag{29a}$$

the dimensionless tensors Γ_m^{ij} are equal to Eqs. (29b)–(29d)

$$\Gamma_{t,in}^{ij} = \sum_{t=1}^{N_{t,in}}\frac{V_t}{V_f}\left(\frac{V_{cv}}{A_{cv}^{jj}}\right)\frac{\ell_{t,i}}{L_t^{eq}} = \frac{1}{\varepsilon A_{cv}^{jj}}\sum_{t=1}^{N_{t,in}}\int_0^1\frac{A_t(\tilde{l})}{c_{td}}\,d\tilde{l}\,\ell_{t,i} \tag{29b}$$

$$\Gamma_{t,o}^{ij} = \sum_{t=1}^{N_{t,o}}\frac{V_t}{V_f}\left(\frac{V_{cv}}{A_{cv}^{jj}}\right)\frac{\ell_{t,i}}{L_t^{eq}} = \frac{1}{\varepsilon A_{cv}^{jj}}\sum_{t=1}^{N_{t,o}}\int_0^1\frac{A_t(\tilde{l})}{c_{td}}\,d\tilde{l}\,\ell_{t,i} \tag{29c}$$

$$\Gamma_p^{ij} = \frac{V_p}{V_f}\frac{1}{\alpha_p}\frac{A_{cv}^{ij}}{\|\bar{A}^j\|} = \frac{\alpha_p^2}{\varepsilon}\frac{A_{cv}^{ij}}{\|\bar{A}^j\|} \tag{29d}$$

Introducing the above results, τ_d^{ij} and D_{ij}^{eff}/D are reduced to Eqs. (30)–(31)

$$\tau_d^{ij} = \left|\left(\chi_{td,in}^j \underbrace{\frac{1}{\varepsilon}\sum_{t=1}^{N_{t,in}}\int_0^1\frac{A_t(\tilde{l})}{c_{td}\,A_{cv}^{jj}}\,d\tilde{l}\,\ell_{t,i}}_{\Gamma_{t,in}^{ij}\leq 1} + \chi_{td,o}^j \underbrace{\frac{1}{\varepsilon}\sum_{t=1}^{N_{t,o}}\int_0^1\frac{A_t(\tilde{l})}{c_{td}\,A_{cv}^{jj}}\,d\tilde{l}\,\ell_{t,i}}_{\Gamma_{t,o}^{ij}\leq 1} + \chi_{pd}^j \underbrace{\frac{\alpha_p^2}{\varepsilon}\frac{A_{cv}^{ij}}{\|\bar{A}^j\|}}_{\Gamma_p^{ij}\leq 1}\right)^{-1}\right| \geq 1 \tag{30}$$

$$\frac{D_{ij}^{\text{eff}}}{D} = \left|\chi_{td,in}^j \underbrace{\sum_{t=1}^{N_{t,in}}\int_0^1\frac{A_t(\tilde{l})}{c_{td}\,A_{cv}^{jj}}\,d\tilde{l}\,\ell_{t,i}}_{\Gamma_{t,in}^{ij}\varepsilon\leq\varepsilon} + \chi_{td,o}^j \underbrace{\sum_{t=1}^{N_{t,o}}\int_0^1\frac{A_t(\tilde{l})}{c_{td}\,A_{cv}^{jj}}\,d\tilde{l}\,\ell_{t,i}}_{\Gamma_{t,o}^{ij}\varepsilon\leq\varepsilon} + \chi_{pd}^j \underbrace{\alpha_p^2\frac{A_{cv}^{ij}}{\|\bar{A}^j\|}}_{\Gamma_p^{ij}\varepsilon\leq\varepsilon}\right| \leq \varepsilon \tag{31}$$

Since $\sum\chi_{d,m}^j \leq 1$ and $\Gamma_m^{ij} \leq 1$, all elements of $\tau_d^{ij} \geq 1$ and $D_{ij}^{\text{eff}}/D \leq 1$. $D_{ij}^{\text{eff}}/D = \varepsilon$ ($\tau_d = 1$) is reached when there are one or more straight fluid elements oriented along j-direction, that is, a porous prismatic CV with ΔC_j prescribed in the axial direction

($\chi_{td}^j = 1$, $c_t = 1$ and $A_t/A_{cv}^{jj} = A_p^j/A_{cv}^{jj} = \varepsilon$). This is the case of the ordered parallelepipedal CV in Fig. 3(b), where the pore space available for transport is perfectly aligned in j-direction (CV faces perpendicular to j-direction are walls). In nanometric materials (e.g., CLs), effective diffusivity, $D_{kn,ij}^{\text{eff}}$, is reduced due to the frequent collision of gas molecules with pore walls (i.e., Knudsen diffusion) [11,14]. Knudsen correction, $f_{kn} = D_{kn,ij}^{\text{eff}}/D_{ij}^{\text{eff}}$, can be incorporated through an additional multiplicative term in Eq. (27d), leading to Eq. (32a)

$$\frac{D_{kn,ij}^{\text{eff}}}{D} = \frac{D_{kn,ij}^{\text{eff}}}{D_{ij}^{\text{eff}}}\frac{D_{ij}^{\text{eff}}}{D} = f_{kn}\frac{D_{ij}^{\text{eff}}}{D}; \quad f_{kn} = \left(1 + \frac{D}{D_{kn}}\right)^{-1} \leq 1; \quad D_{kn} = \frac{R_{t,p}^{\text{avg}}}{3}\sqrt{\frac{8R^oT}{\pi M_g}} \tag{32a}$$

where D^{kn} is the Knudsen diffusivity derived from kinetic theory of gases, R^o is the ideal gas constant, T is the operating temperature, M_g is the gas molecular mass, and R_t^{avg} and R_p^{avg} are the throat and pore average radii, $R_t^{\text{avg}} = (R_t^{\text{fcv}} + R_t^{\text{fpb}})/2$ and $R_p^{\text{avg}} = [3V_p/(4\pi)]^{1/3}$, respectively. The effect of $R_{t,p}^{\text{avg}}$ on f_{kn} is dominant in most situations involving small temperature and pressure variations [14,114].

The dependency of $D_{kn,ij}^{\text{eff}}/D$ on $R_{t,p}^{\text{avg}}$ mainly modifies: (*i*) the concentration partition coefficients, $\chi_{d,m}^j$, and (*ii*) the contribution of t and p to $D_{kn,ij}^{\text{eff}}/D$ (neglecting the local effect on the shape factor c_{td}). The corrected D_{ij}^{eff}/D tensor is equal to Eq. (32b)

$$\frac{D_{ij}^{\text{eff}}}{D} = \chi_{kn,in}^j \sum_{t=1}^{N_{t,in}} f_{t,in}^{kn} \int_0^1 \frac{A_t(\tilde{l})}{c_t A_{cv}^j}\, d\tilde{l}\, \ell_{t,i} + \chi_{kn,o}^j \sum_{t=1}^{N_{t,o}} f_{t,o}^{kn} \int_0^1 \frac{A_t(\tilde{l})}{c_t A_{cv}^j}\, d\tilde{l}\, \ell_{t,i} + \chi_{kn,p}^j f_p^{kn}\alpha_p^2 \frac{A_{cv}^{ij}}{\|\bar{A}^j\|} \leq 1 \tag{32b}$$

where $\chi_{kn,m}^j$ ($m = t, in; t, o; p$) is the concentration partition coefficient determined with diffusive conductances incorporating Knudsen correction ($G = (DA/L^{eq})f_{kn}$).

The nanoscale correction can be included in all diffusivity calculations regardless of the characteristic pore size of the examined TPM, since $f_{kn} \to 1$ for pore sizes in the order of micrometers [14].

4.2. Absolute permeability

According to Darcy's law, the absolute permeability tensor in creeping regime is given by Eq. (33a)

$$K_{ij}^{\text{eff}} = \frac{\mu L_{cv}^{jj}}{V_{cv}\Delta p_j}\left(\sum_{t=1}^{N_t} V_t u_{t,i} + V_p u_{p,i}\right); \quad u_{t,i} = \frac{K_t}{\mu}\frac{\Delta p_t}{L_t^{eq}}\ell_{t,i}; \quad u_{p,i} = \frac{K_p}{\mu}\frac{\Delta p_p}{L_p^{eq}}\ell_{p,i} \tag{33a}$$

where μ is the dynamic viscosity, $\Delta p_t, \Delta p_p$ is the pressure difference across t, p, and $u_{t,i}, u_{p,i}$ is the *i*-component of the interstitial velocity in t, p. K_{ij}^{eff} is independent of μ as given by Darcy's law [2].

Considering Carman-Kozeny analysis [115], (33a) can be expressed in terms of the characteristic permeability of the fluid network, K_f, leading to Eq. (33b)

$$\frac{K_{ij}^{\text{eff}}}{K_f} = \sum_{t=1}^{N_t}\frac{K_{t,ij}^{\text{eff}}}{K_f} + \frac{K_{p,ij}^{\text{eff}}}{K_f}; \quad \frac{K_{t,ij}^{\text{eff}}}{K_f} = \frac{\varepsilon_t}{\tau_{th}^{ij}}; \quad K_f = \frac{d_h^2}{16k_o}; \quad d_h = \frac{4\varepsilon}{a} \tag{33b}$$

where k_o is the cross-sectional shape factor derived from Darcy's friction factor ($k_o = 2$ for circular throats), and d_h is the volume-average hydraulic diameter, with a a specific surface area (per unit total volume). The effective permeability tensor, K_{ij}^{eff}/K_f, takes the expanded form of Eq. (33c) (similar to D_{ij}^{eff}/D)

$$\frac{K_{ij}^{\text{eff}}}{K_f} = \chi_{th,in}^j \sum_{t=1}^{N_{t,in}}\frac{K_t}{K_f}\int_0^1 \frac{A_t(\tilde{l})}{c_t A_{cv}^j}\, d\tilde{l}\, \ell_{t,i} + \chi_{th,o}^j \sum_{t=1}^{N_{t,o}}\frac{K_t}{K_f}\int_0^1 \frac{A_t(\tilde{l})}{c_t A_{cv}^j}\, d\tilde{l}\, \ell_{t,i} + \chi_{ph}^j\frac{K_p}{K_f}\alpha_p^2\frac{A_{cv}^{ij}}{\|\bar{A}^j\|} \tag{33c}$$

where K_t and K_p are the hydraulic permeability of t and p, respectively. The pressure partition coefficient, $\chi_{h,m}^j = \Delta p_m/\Delta p_j$ ($m = t, in; t, o; p$), is obtained from mass conservation in the equivalent resistor network of hydraulic conductances. For incompressible flow, we can write Eq. (33d)

$$\Delta p_{t,in} \sum_{t=1}^{N_{t,in}} G_{th,in}^j = \Delta p_{t,o} \sum_{t=1}^{N_{t,o}} G_{th,o}^j; \quad \Delta p_{t,in} \sum_{t=1}^{N_{t,in}} G_{th,in}^j = \Delta p_p G_{ph}^j \tag{33d}$$

where the hydraulic conductances of t and p for Δp_j are equal to Eqs. (33e)–(33f) (considering $k_o = 2$ for both t and p in a first approximation)

$$G_{th}^j = \frac{K_t A_{t,in/o}^{\text{ref}}}{\mu L_t^{eq}}; \qquad K_t = \frac{d_{h,t}^2}{16k_o}, \quad d_{h,t} = 2R_t^{\text{fcv}} \tag{33e}$$

$$G_{ph}^j = \frac{K_p A_p^{jj}}{\mu L_p^{jj}} = \alpha_p \frac{K_p}{\mu} \frac{A_{cv}^{jj}}{L_{cv}^{jj}}; \quad K_p = \frac{d_{h,p}^2}{16k_o}, \quad d_{h,p} = 2R_p = 2\left(\frac{3V_p}{4\pi}\right)^{1/3} \tag{33f}$$

The addition of a distributed hydraulic resistance, $G_{h,\text{int}}^j$, in the calculation of the partition coefficients can be performed in the same way as for diffusion.

Unlike diffusive tortuosity, hydraulic tortuosity cannot be directly extracted from the calculations due to the absence of a universal relationship between permeability, K_{ij}, hydraulic tortuosity, $\tau_{h,ij}^2$, and microstructural parameters (e.g., porosity, ε) without fitting parameters. Indeed, the value of the Carman-Kozeny constant, K_{ck}^{ij}, and $\tau_{h,ij}^2$ are both unknowns in the Carman-Kozeny equation, so the determination of one is necessary to calculate the other. Here, the approach proposed by Duda et al. [116,117] to determine the hydraulic tortuosity based on the magnitude-to-component velocity ratio was used, as given by Eq. (34a)

$$\tau_h^2 = \frac{\langle \|\bar{u}\|^j \rangle}{\langle \bar{u}_i^j \rangle} = \begin{vmatrix} \frac{\langle \|\bar{u}\|^x \rangle}{\langle u_x^x \rangle} & \frac{\langle \|\bar{u}\|^y \rangle}{\langle u_x^y \rangle} & \frac{\langle \|\bar{u}\|^z \rangle}{\langle u_x^z \rangle} \\ \frac{\langle \|\bar{u}\|^x \rangle}{\langle u_y^x \rangle} & \frac{\langle \|\bar{u}\|^y \rangle}{\langle u_y^y \rangle} & \frac{\langle \|\bar{u}\|^z \rangle}{\langle u_y^z \rangle} \\ \frac{\langle \|\bar{u}\|^x \rangle}{\langle u_z^x \rangle} & \frac{\langle \|\bar{u}\|^y \rangle}{\langle u_z^y \rangle} & \frac{\langle \|\bar{u}\|^z \rangle}{\langle u_z^z \rangle} \end{vmatrix} \geq 1 \tag{34a}$$

where $\|\bar{u}\|^j$ and u_i^j are the velocity magnitude and the i-component of the velocity vector for Δp_j, respectively, and $\langle \pi \rangle = (1/V_{cv}) \int_{V_{cv}} \pi \, dV$ is the volume average operator. K_{ck}^{ij} can be directly extracted from the computed values of K_{ij} and τ_{ij}^2 [42,115], according to Eq. (34b)

$$K_{ij} = \frac{\varepsilon^3}{K_{ck}^{ij} \tau_{ij}^2 a} \Rightarrow K_{ck}^{ij} = \frac{\varepsilon^3}{K_{ij} \tau_{ij}^2 a} \tag{34b}$$

In nanometric materials, the viscous resistance of gases decreases due to the presence of a slipping boundary condition at pore walls when the mean free path, λ, is comparable to the pore radius, $R_{t,p}^{\text{avg}}$ [118]. This nanoscale effect can be incorporated on top of Poiseuille's flow by introducing a molecular correction factor, F_{kn} – a rather similar approach to Knudsen diffusion. For incompressible flow, we yield Eq. (35a) [119]

$$\bar{u} = \frac{K_{t,p}}{\mu} \frac{\Delta p_{t,p}}{L_{t,p}^{eq}} F_{kn}; \quad F_{kn} = 1 + \frac{4c\lambda}{R_{t,p}^{\text{avg}}} \tag{35a}$$

where c is a collision proportionality factor ($c \simeq 1$). According to the kinetic theory of gases, λ depends on viscosity, temperature and average pressure, p^{avg}, according to Eq. (35b)

$$\lambda = \sqrt{\pi/2} \sqrt{\frac{R^o T}{M_g}} \frac{\mu}{p^{\text{avg}}} \tag{35b}$$

The corrected permeability tensor, K_{ij}^{eff}/K_f, is equal to Eq. (35c)

$$\frac{K_{ij}^{\text{eff}}}{K_f} = \chi_{sl,in}^j \sum_{t=1}^{N_{t,in}} F_{t,in}^{kn} \frac{K_t}{K_f} \int_0^1 \frac{A_t(\tilde{l})}{c_t A_{cv}} d\tilde{l} \ell_{t,i} + \chi_{sl,o}^j \sum_{t=1}^{N_{t,o}} F_{t,o}^{kn} \frac{K_t}{K_f} \int_0^1 \frac{A_t(\tilde{l})}{c_t A_{cv}^j} d\tilde{l} \ell_{t,i} + \chi_{sl,p}^j F_p^{kn} \frac{K_p}{K_f} \alpha_p^2 \frac{A_{cv}^{ij}}{\|\bar{A}^j\|} \tag{35c}$$

where $\chi_{sl,m}^j$ ($m = in; o; p$) is the pressure partition coefficient determined with hydraulic conductances accounting for the slippage correction ($G = (KA^{\text{ref}}/L^{eq})F^{kn}$).

When pressure can be assumed constant ($p \simeq p^{\text{avg}}$), F_{kn} can be taken into account for porous media of any pore size, since $F_{kn} \to 1$ for pore sizes above 1 μm (as in the case of f_{kn}). However, in applications where p^{avg} cannot be assumed constant, the nonlinear dependency between $\bar{u}$ and Δp introduced by $F_{kn}(p)$ must be included at the CV scale using Kirchhoff's transformation. Considering the linearized potential of Eq. (35d)

$$\Theta = \int_0^p F^{kn}(\eta) \, d\eta = \int_0^p 1 + \frac{4c}{R_f} \left(\sqrt{\pi/2} \sqrt{\frac{R^o T}{M_g}} \frac{\mu}{\eta} \right) d\eta, \tag{35d}$$

we yield Eq. (35e) at the CV scale to be solved numerically in a CFD solver

$$\nabla \cdot \left(-\frac{K_{ij}^{\text{eff}}}{\mu} \nabla\Theta \right) = 0 \tag{35e}$$

where K_{ij}^{eff} is the permeability tensor determined without the nanoscale correction factor (Eq. (33a)), and R_f is the average CV pore radius (see Section 3).

The pressure field with the nanoscale correction factor can be determined through the inverse Kirchhoff's transformation by solving Eq. (35f)

$$\Theta^{\text{cfd}} - \int_0^{p^{\text{cfd}}} F^{kn}(\eta)\,\mathrm{d}\eta = \int_0^p 1 + \frac{4c}{R_f}\left(\sqrt{\pi/2}\sqrt{\frac{R^oT}{M_g}}\frac{\mu}{\eta}\right)\mathrm{d}\eta = 0 \to p^{\text{cfd}} \tag{35f}$$

It is worth noting that the present method allows the combination of non-linear effects and spatially-varying microstructural properties at the CV scale (e.g., specific surface area, radius, porosity, coordination number, etc.) during the calculation of inverse Kirchhoff's transformation in a CFD code. Although possible, the incorporation of non-linear effects at the sub-CV scale is not convenient because calculated effective properties depend on the actual pressure, complicating the data export methodology.

For applications at Reynolds numbers higher than one (based on the average pore/solid diameter), the non-linear dependency between $\bar{u}$ and Δp beyond Darcy's regime can be important. The so-called Forchheimer equation is given by (36) [120]

$$\nabla p = -\frac{\mu}{K_{ij}^{\text{eff}}}\bar{u} - C_F\rho\|\bar{u}\|\bar{u} \Rightarrow \bar{u} = -\left(\frac{\mu}{K_{ij}^{\text{eff}}} + C_F\rho\|\bar{u}\|\right)^{-1}\nabla p \tag{36}$$

where $\|\bar{u}\|$ is the magnitude of the superficial velocity vector. In CFD simulations, the Forchheimer constant, C_F, may be expressed as a function of local microstructural properties using correlations determined from DNS at a finer scale (see, e.g., [121–123]).

4.3. Solid-phase effective conductivity tensor

The solid-phase conductivity (electrical, ionic or thermal conductivity) can be extracted from the solid network considering also a Laplace-like conservation equation [5]. However, the more intricate topology of the solid network complicates the extraction of effective transport properties based on a 3D analysis. The main drawbacks are: (*i*) the lack of a clear criterion to determine inlet and outlets depending on the *j*-direction under analysis due to the absence of a central conductive element, and (*ii*) the presence of a no-flux boundary condition at solid-pore interfaces rather than a Dirichlet boundary condition. The analysis of the solid phase can be simplified by working independently on each solid node *ns* (see Fig. 2), and then averaging the effective conductivity among all solid nodes. The calculation on each solid node can be performed using a 1D continuum approximation to account for the volume reduction originated by fluid throats. This approach is a reasonable approximation for analyzing the solid phase given the relevance that contact resistances often play in solid conduction and the irregular arrangement of solid matrices (especially in the case of multi-component TPM) [17]. More elaborated models could be implemented by complementing the method with DNS and machine learning.

According to Fourier's or Ohm's laws, the effective conductivity tensor is given by the volume-average flux in a CV, $\bar{j}_s^{\text{avg}}$, divided by the macroscopic scalar gradient in *j*-direction, $\Delta s_j/L_{cv}^{jj}$. An arrangement of CV partitions throughout the solid network must be assumed. For simplicity, we shall consider a parallel arrangement of CV partitions, so that the macroscopic flux in each CV partition is proportional to $\Delta s_j/L_{cv}^{jj}$. Moreover, the central pore body can be removed from the analysis, since the internal flux $\bar{j}_s$ is null therein. Introducing these simplifications, the normalized solid-phase conductivity, S_{ij}^{eff}/S, is directly given by the volume-average effective conductivity of each solid node *ns* (see Eq. (37a))

$$\frac{S_{ij}^{\text{eff}}}{S} = \frac{j_s^{\text{avg}}}{\Delta s_j/L_{cv}^{jj}} = \frac{L_{cv}^{jj}}{V_{cv}\Delta s_j}\sum_{ns=1}^{N_t} V_{ns}\left.\frac{S_{ij}^{\text{eff}}}{S}\right|_{ns}\frac{\Delta s_j}{L_{cv}^{jj}} \Rightarrow \frac{S_{ij}^{\text{eff}}}{S} = \frac{1}{V_{cv}}\sum_{ns=1}^{N_t} V_{ns}\left.\frac{S_{ij}^{\text{eff}}}{S}\right|_{ns} \tag{37a}$$

where S and s are the bulk property and the scalar under analysis, and V_{ns} and $\left.S_{ij}^{\text{eff}}/S\right|_{ns}$ are the volume and normalized effective conductivity of *ns*, respectively.

For a given *j*-direction, the flux $\bar{j}_{ns}$ can be quantified by the average flux between all face pairs *ps* preferentially oriented in that direction. The *i*-component takes the form of Eq. (37b)

$$j_{ns,i}^j = \frac{\chi_{ns}^j}{N_{ps}^j}\sum_{ps=1}^{N_{ps}^j} S\frac{\Delta s_j}{L_{ps}^{eq,j}}|\ell_{ps,i}|, \tag{37b}$$

leading to Eq. (37c) for $\left.S_{ij}^{\text{eff}}/S\right|_{ns}$

$$\left.\frac{S_{ij}^{\text{eff}}}{S}\right|_{ns} = \frac{j_{ns,i}^j}{S\Delta s_j/L_{ns}^j} = \frac{\varepsilon_{ns}^{2/3}\chi_{ns}^j}{N_{ps}^j}\sum_{ps=1}^{N_{ps}^j}|\ell_{ps,i}| \tag{37c}$$

where L_{ns}^j is the equivalent length of node *ns* under bulk conditions without fluid throats ($L_{ns}^j/L_{ps}^{eq,j} = \varepsilon_{ns}^{2/3}$), χ_{ns}^j is the partition coefficient of *ns*, N_{ps}^j is the number of face pairs in *j*-direction corresponding to *ns*, and $|\ell_{ps,i}|$ is the absolute value of the *i*-component of the unit direction vector between the centroids of solid pair *ps*. Note that all elements of $\left.S_{ij}^{\text{eff}}/S\right|_{ns} \leq 1$, since $\chi_{ps}^j \leq 1$, $|\ell_{ps,i}| \leq 1$ and $\varepsilon_{ns} \leq 1$.

The partition coefficient χ_{ps}^j is obtained from flux rate conservation in j-direction between solid node ns and a distributed contact conductance, $G_{s,\text{int}}^j$, placed in series (see Eq. (38))

$$\chi_{ns}^j = \frac{G_{s,\text{int}}^j}{G_{ns}^j}; \quad G_{ns}^j = \frac{SA_{ns}^{\text{ref},j}}{L_{ns}^{eq,j}} \quad A_{ns}^{\text{ref},j} = \frac{1}{N_{ps}^j} \sum_{np=1}^{N_{ps}^j} A_{ps}^{\text{ref},j}, \ L_{ps}^{eq,j} = \frac{1}{N_{ps}^j} \sum_{ps=1}^{N_{ps}^j} L_{ps}^{eq,j} \tag{38}$$

where $A_{ns}^{\text{ref},j}$ and $L_{ns}^{eq,j}$ are the mean reference area and equivalent length among all solid pairs ps in ns, respectively.

The analysis of multi-component TPM is straightforward using the above formulation. The only modification is that the volume fraction of the corresponding solid phase k, ϵ_{ns}^k, must be considered. As a result, the volume-averaging weights in (37a), and the equivalent length ratio $L_{ns}^j/L_{ps}^{eq,j}$ and partition coefficient in (37c) change depending on the composition of solid node ns.

5. Implementation methodology

The main features of the implementation methodology of *POREnet* based on the methods presented in the previous sections are summarized in Fig. 4. The flow chart can be decomposed into five steps:

Step 1. Generation of continuum CV tessellation. A CV tessellation is generated. As commented in Section 2, infinitely many tessellations can be considered either based on ordered or random CVs to describe spatially-varying properties of a TPM. Polyhedral Voronoi tessellation based on seed point generation provides a widespread, versatile framework. In multi-region TPMs, several regions can be incorporated via bounding box identification. Sub-regions are added sequentially on top of a "background" region that spans the entire domain. The multi-layer approach ensures that the full modeled domain is covered by tessellated CVs.

Step 2. Extraction of fluid and solid networks on a CV basis. A pore-throat geometry of pore space within each CV is generated, which is composed of a central pore body geometrically similar to the CV and truncated conical throats connected to every CV face. The solid network encompasses the surrounding shapeless space in a CV, which is subdivided into solid nodes or partitions to facilitate subsequent calculations. Voronoi cells are uniquely defined by their conforming vertices and co-planar faces. Geometrical information (e.g., volumes, unit direction vectors, areas, inlet/outlet labels, etc.) is determined through a mixture of numerical and analytical operations to reduce computational time. Geometrical parameters can be adjusted to modify properties, such as porosity, throat conicity and spatial composition of multi-component materials, among others.

Step 3. Calculation of effective properties on a CV basis. Microstructural properties of every CV (porosity, specific surface area, coordination number, anisotropy ratio, average pore radius, etc.) are determined using the geometrical descriptors extracted in Step 2. Effective transport property tensors (mass diffusivity, permeability, and solid-phase conductivity), entry capillary pressure and contact angle are computed by means of: (*i*) tensorization of volume average fluxes of fluid and solid networks, and (*ii*) empirical, numerical or semi-empirical correlations expressed as a function of local microstructural properties. 3D tensorization requires a CV metric to account for the alteration of bulk, isotropic space originated in a tessellated CV with inlets and outlets, thus providing an adequate reference to normalize discrete transport resistances. Correlation of local effective properties is useful to model fine regions of multiscale TPM assemblies with large disparity of scales (e.g., MPL+GDL). Calculated microstructural and transport properties are stored both on a CV basis and on a voxel basis for subsequent manipulation with image processing techniques.

Step 4. Addition of sub-CV features on a voxel basis. Interfacial regions and defects in porous assemblies are frequently found in TPM. Microstructural and transport properties with a resolution lower than the CV size can be added on a voxel basis using image processing. Voxel-scale operations can be performed through direct manipulation of previously saved matrices, such as addition of mixed interfacial properties and cracks in a selected bounding box or superimposition of macroscopic features from ex-situ images. In addition, the modeled domain can be enlarged by replicating an originally generated sample stochastically in the material plane. Stochastic replication is a powerful approach for upscaling the area of a domain up to one order of magnitude with a much lower computational time than direct generation through Steps 1-3. Communication with external image processing softwares (e.g., Fiji [124]) is not currently supported but can be useful for fast application of filters, boolean operations, etc.

Step 5. Data saving, mesh interpolation and CFD modeling. Data are saved on 3D image stacks with single precision. Anisotropic voxel sizes can be specified by introducing a scaling parameter of order unity in x, y, z-space on cubic voxels. Image scaling assumes that pore-scale composition is similar in larger CVs, an approach that can be used to enclose larger computational domains with reduced spatial resolution of heterogeinities. Previously extracted effective properties remain unchanged at this step. Other formats to export voxelized data are possible, such as binary ASCII files. Interfacial CV-CV properties (e.g., discrete entry capillary pressure between CVs) must always be exported to binary ASCII files as a sparse adjacency matrix based on CV identifiers. Saved image data are interpolated to centroid coordinates of a computational mesh (exported from the CFD solver). A fast k-nearest neighbor algorithm can be used when image and mesh resolutions are similar. The interpolated data are saved on a binary ASCII file to be read in the CFD solver (e.g., via user defined functions programmed in C language for ANSYS Fluent). Simulation of linear and non-linear Laplace equations can be carried out depending on the capabilities of the CFD software. Solution of other types of equations (e.g., Forchheimer term in Navier-Stokes equations)
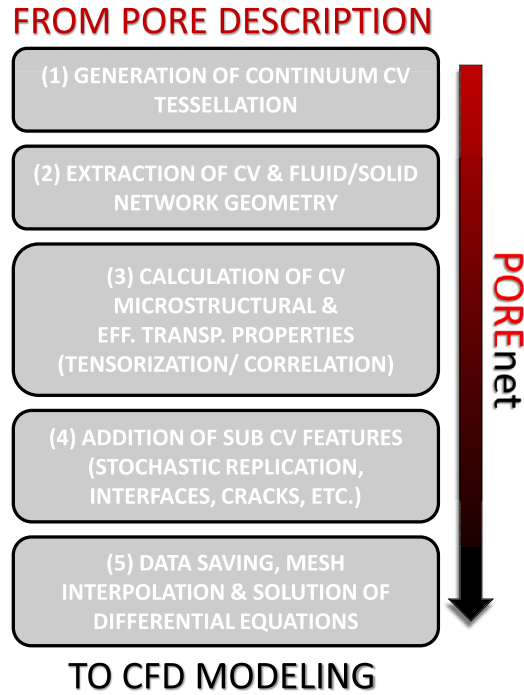
FROM PORE DESCRIPTION

(1) GENERATION OF CONTINUUM CV TESSELLATION

(2) EXTRACTION OF CV & FLUID/SOLID NETWORK GEOMETRY

(3) CALCULATION OF CV MICROSTRUCTURAL & EFF. TRANSP. PROPERTIES (TENSORIZATION/ CORRELATION)

(4) ADDITION OF SUB CV FEATURES (STOCHASTIC REPLICATION, INTERFACES, CRACKS, ETC.)

(5) DATA SAVING, MESH INTERPOLATION & SOLUTION OF DIFFERENTIAL EQUATIONS

POREnet

TO CFD MODELING

Fig. 4. Flow chart of the implementation methodology of *POREnet*. From a tessellated pore-scale description of a TPM, local effective transport properties are extracted toward the solution of differential conservation equations in a CFD solver.

is also possible if effective transport properties are not obtained from a tensorization method but from a local correlation with microstructural properties. CFD simulations can be used to either compute overall effective transport properties in a full TPM domain or to perform more realistic multiphysics, multiphase, multiscale simulations.

6. Results

The modeling approach was tested against a collection of cases extracted from electrochemistry due to the variety of transport processes and extended use of TPM (see, e.g., [5,6,125]). As listed in Table 1, four case studies were analyzed: (*i*) a GDL with a cracked MPL, as those frequently used in PEMFCs [125]; (*ii*) a macroporous electrode with a bimodal pore size distribution, as those investigated in RFBs [13,126]; (*iii*) a CL of a PEMFC, as an example of a fuel cell or battery microporous electrode [11,12,14,60]; and (*iv*) an ion-exchange membrane (e.g., Nafion in protonated form), as an example of non-linear mesoscopic modeling at nanoscale [4, 127]. The average pore radii of the different TPM are: (*i*) GDL+MPL, $R_f \approx 11$ μm + 150 nm, (*ii*) bimodal macroporous electrode, $R_{f,1} \approx 9$ μm and $R_{f,2} \approx 17.5$ μm, (*iii*) CL, $R_f \approx 37$ nm, and (*iv*) membrane, $R_f \approx 4$ nm. The sample area was set around one order of magnitude larger than the average pore size. The thickness was determined either according to the finite size of the modeled material or to reduce computational time in a REV (e.g., CL and membrane). No attempt was made here to model domains with large pore populations, such as a single electrochemical cell or a CL along the full thickness. The transport properties of the macroporous electrode, CL and membrane were generated using exclusively the tensorization method presented in Section 4, even though only R_f was used for mesoscopic modeling of the membrane. Isotropic microstructural properties were considered in the regional generation process of the various samples using a random Voronoi tessellation. For the multiscale GDL+MPL assembly, the transport properties of the macroporous GDL were also calculated using the tensorization method but modifying the random CV tessellation to obtain more anisotropic properties with preferential alignment in the in-plane direction. The fine pore structure of the MPL was reproduced using a random, isotropic CV tessellation with an average size 5 times smaller than the GDL, $N_p = 2.5 \times 10^4$ pores in each CV, and reducing the pore size by a factor $S_p = 18$ with respect to the value used for the tessellation. MPL properties were correlated as a function of local porosity. The above variety of generation routes allowed us to assess the correct functioning of the algorithm in a wide range of scenarios. ANSYS Fluent was selected as the CFD solver. Only the diagonal elements of the property tensors were considered in the simulations due to the larger numerical stability.

The simulation campaign spanned around 400 simulations, completed over the course of 1-2 days using a conventional workstation with 12 processors and 128 GB RAM memory. For the GDL+cracked MPL, diffusivity and two-phase IP simulations were run for 15 MPL crack volume fractions, $\varepsilon_{\mathrm{crack}}^{\mathrm{mpl}}$, ranging between $\varepsilon_{\mathrm{crack}}^{\mathrm{mpl}} \approx 0 - 0.1$ with 8 realizations per value (120 simulations). Crack density was modified by varying the number of seed points used to mimic the crack geometry from edges of Voronoi cells. For the macroporous electrode, permeability calculations were run for 21 secondary macropore volume fractions, $\varepsilon_{\mathrm{macro}}$, varying between $\varepsilon_{\mathrm{macro}} \approx 0 - 0.6$ with 5 realizations (105 simulations). The secondary volume fraction was augmented by increasing the number of

Table 1

Case studies examined for model testing: (*i*) GDL+cracked MPL, (*ii*) macroporous electrode, (*iii*) CL (i.e., microporous electrode), and (*iv*) ion-exchange membrane. It is indicated the average pore radius, the sample area and thickness, the examined physical variable and the corresponding model variable used to modify it, the analyzed range, and the number of values and realizations (per value) simulated in each case study. For the macroporous electrode, the average pore radius of the secondary macropore region is included between brackets.

Case study	Average pore radius	Area	Thickness	Physical variable	Model variable	Range	Number of values (realizations)
GDL+cracked MPL	11 μm + 150 nm	1.5×1.5 mm^2	250 μm	Cracks volume fraction	Cracks seed points	0–0.1	15 (8)
Macroporous electrode	9 μm (17.5 μm)	1.5×1.5 mm^2	500 μm	Secondary macroporous volume fraction	Secondary cylindrical sub-regions	0–0.6	21 (5)
Catalyst layer (microporous electrode)	37 nm	3×3 μm^2	1 μm	Porosity (component fraction)	Pore scaling factor	0–0.8 (0-0.5)	24 (5)
Ion-exchange membrane	4 nm	600×600 nm^2	200 nm	Relative humidity	–	0.1–1+water ($s = 0.4$)	6 (10)

cylindrical sub-regions preferentially aligned in the material plane. For the CL, diffusivity and conductivity simulations were run for 24 electrode porosities ($\varepsilon \approx 0 - 0.8$) and 5 realizations, considering three multi-component solid compositions ($\varepsilon_{k,s} = 0.5, 0.3, 0.2$), i.e., variable component volume fraction (per unit total volume) between $\varepsilon_k \approx 0 - 0.5$ (120 simulations). The electrode porosity was modified using the pore scaling factor α_p. For the membrane, only the operating relative humidity (RH) was examined and no material parameters were further adjusted. Mesoscopic diffusivity and conductivity simulations were run for 6 humidifications, RH = 0.1, 0.2, 0.4, 0.6, 0.8 and RH = 1+liquid water (saturation, $s = 0.4$), with 20 realizations per value (120 simulations).

According to Eq. (39a), normalized effective properties in the full sample (either diffusivity, permeability or conductivity), $\Pi_{jj}^{\mathrm{eff}}/\Pi$, were determined by volume averaging the flux in j-direction, J_j, subjected to Dirichlet boundary conditions with a scalar difference $\Delta \pi_j$ – no-flux boundary conditions were prescribed in the remaining surfaces

$$\frac{\Pi_{jj}^{\mathrm{eff}}}{\Pi} = \frac{\frac{1}{V} \int_V J_j \, \mathrm{d}V}{\frac{\Delta \pi_j}{L_j}} \tag{39a}$$

where L_j is the sample length in j-direction.

For two-phase simulations, IP was evolved from an initial random saturation distribution imposed on the first two rows of the cells facing the inlet surface [16,30]. A standard IP algorithm without trapping was implemented in parallel based on the adjacency matrix using user defined functions in ANSYS Fluent [30]. Liquid pressure, p_l, was subsequently determined by solving two-phase Darcy's equation on the percolated water path. This approach emulates quasi-steady-state transport of water at low capillary number ($Ca \ll 1$) [30]. In a first approximation, $s = 1$ was set for macroporous features above 1 μm and $s = 0.5$ for microscopic features below 1 μm owing to the larger entry pressure and gradual pore filling in the latter. A more detailed formulation could be included using semi-empirical retention curves or a bundle of capillary tubes sub-model to relate capillary pressure with local saturation, p_c–s relationship [77]. By definition, average saturation on a sample was calculated as the ratio of water volume, V_w, to total volume, V, throughout all computational cells, according to Eq. (39b)

$$s_{\mathrm{avg}} = \frac{V_w}{V} = \frac{\sum s \, \varepsilon V_{\mathrm{cell}}}{\sum \varepsilon V_{\mathrm{cell}}} \tag{39b}$$

where ε and V_{cell} are the local porosity and volume of a mesh cell, respectively.

A structured, hexahedral mesh was used in all case studies examined. The mesh resolution was determined from a grid independence study, where the cell size was gradually decreased by a factor of two. The initial cell size was set five times lower than the average pore size of the corresponding TPM under analysis (minimum pore size in the case of bimodal porous media). Resolution-independent results with a variation lower than 1% were reached with a cell size one order of magnitude lower than the corresponding average pore size. This level of accuracy resulted in computational meshes with around one million of cells, providing a fine spatial description of heterogeinities and virtually equal volume average effective transport properties.

Fig. 5(a)–(b) shows the results from the analysis of the GDL+cracked MPL conducted under both dry and partially-saturated conditions. Representative distributions of the effective diffusivity in wet condition, saturation and liquid-phase pressure are shown in Fig. 5(c). The normalized dry effective diffusivity of the MPL, $f(\varepsilon) = D_{\mathrm{dry}}^{\mathrm{eff}}/D$, was modeled by an isotropic power-law function of the form of Eq. (40) [128–130]

$$f_{\mathrm{mpl}}(\varepsilon) = \varepsilon^2 f_{kn} \tag{40}$$
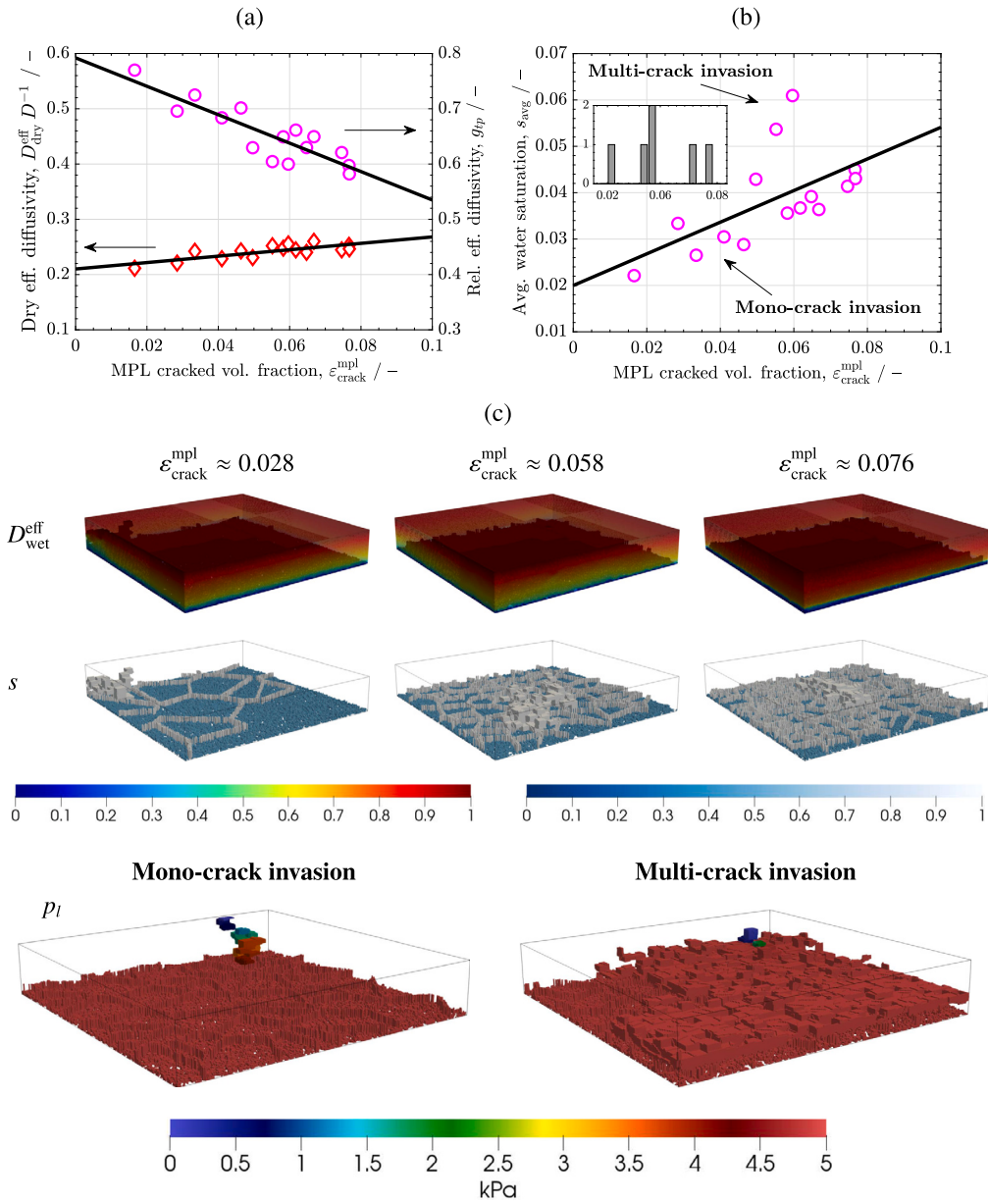
Fig. 5. Variation of (a) both normalized through-plane dry effective diffusivity, $f_{tp} = D_{dry}^{eff} D^{-1}$, and relative effective diffusivity, $g_{tp} = D_{wet}^{eff} (D_{dry}^{eff})^{-1}$, and (b) average water saturation, s_{avg}, as a function of volume fraction of cracks, $\varepsilon_{crack}^{mpl}$. The inset shows the number of cases with significant multi-crack invasion patterns. Mono-crack invasion is more frequent at low crack density, and increases for middle and high crack densities. (c) Distributions of (up) normalized gas species concentration and water saturation, corresponding to wet diffusivity and invasion-percolation simulations at different $\varepsilon_{crack}^{mpl}$, and (down) liquid-phase pressure, p_l, corresponding to mono-crack ($s_{avg} \approx 0.03$) and multi-crack ($s_{avg} \approx 0.16$) invasion patterns at $\varepsilon_{crack}^{mpl} \approx 0.055$.

where the local porosity of the MPL varied between $\varepsilon_{mpl} \approx 0.2 - 0.6$ in microporous regions (lower than that of the macroporous GDL, $\varepsilon_{gdl} \approx 0.6 - 0.85$) and $\varepsilon_{crack} = 1$ in cracked volume space. The Knudsen correction factor is given by Eq. (32a), considering the molecular mass of oxygen.

The saturation exponent of the local relative effective diffusivity, $g_{local}(s)$, was fixed to $n = 3$, according to the previous numerical results of García-Salaberri et al. [9] (see Eq. (41))

$$g(s) = (1 - s)^3 \tag{41}$$

where s is the local saturation.

The entry capillary pressures of both the GDL and the MPL were modeled based on Washburn equation (Eq. (15a)) with $\theta_t = 100°$. Other scenarios shall be examined, e.g., considering Purcell equation for the GDL (Eq. (15b)).

The computed data were averaged among all sample realizations and fitted to mathematical expressions (see black lines in Fig. 5(a)–(b)). According to Eqs. (42a)–(42c), the variation of the normalized dry effective diffusivity and the relative effective diffusivity, $f_{tp} = D^{\text{eff}}_{\text{dry}} D^{-1}$ and $g_{tp} = D^{\text{eff}}_{\text{wet}} (D^{\text{eff}}_{\text{dry}})^{-1}$, and the average water saturation, s_{avg}, with the crack volume fraction, $\varepsilon^{\text{mpl}}_{\text{crack}}$, are well fitted (on average) by linear expressions (Fig. 5(a)–(b))

$$f_{tp} = \frac{D^{\text{eff}}_{\text{dry}}}{D} = 0.21 + 0.58\, \varepsilon^{\text{mpl}}_{\text{crack}} \quad R^2 = 0.77 \tag{42a}$$

$$g_{tp} = \frac{D^{\text{eff}}_{\text{wet}}}{D^{\text{eff}}_{\text{dry}}} = 0.8 - 2.6\varepsilon^{\text{mpl}}_{\text{crack}} \qquad R^2 = 0.62 \tag{42b}$$

$$s_{\text{avg}} = 0.02 + 0.34\varepsilon^{\text{mpl}}_{\text{crack}} \qquad R^2 = 0.4 \tag{42c}$$

The rather low R^2 obtained for s_{avg} is explained by stochastic variations between mono-crack and multi-crack invasion patterns (see picture at the bottom part of Fig. 5(c)). Multi-crack invasion arises when the crack density is increased due to the higher probability of finding cracks that are connected to GDL regions with low entry capillary pressure. As shown in the inset of Fig. 5(b), the frequency of multi-crack invasion events correlates positively with the number of cracks in the MPL, since the low entry capillary pressure in cracks provides preferential paths for water transport [131,132]. Multi-crack invasion mimics flooding-related issues observed in MPL+GDL assemblies with excessive defects between layers (e.g., due to inter-layer delamination), where water can block a significant fraction of transport pathways between the channel and the CL [133]. Unlike the low average saturations reached in mono-crack invasion ($s_{\text{avg}} \approx 0.02 - 0.04$), average water saturations around $s_{\text{avg}} \approx 0.04 - 0.06$ are reached in multi-crack invasion

In terms of diffusion, a higher crack volume fraction leads to two opposite effects. At dry condition, a larger number of cracks slightly facilitates diffusion across the MPL+GDL assembly, since diffusivity in cracked void space ($D^{\text{eff}}_{\text{dry}}/D \approx 1$) is significantly larger than diffusivity in MPL nanometric regions ($D^{\text{eff}}_{\text{dry}}/D \approx 0.1 - 0.2$). Note that Knudsen effect reduces even further the effective diffusion coefficient at pore scales below 1 μm [14]. However, the situation is reversed under two-phase conditions due to the increase of average saturation with crack volume fraction, regardless of the invasion mode (mono-crack vs. multi-crack invasion). The increase of both dry effective diffusivity and water saturation reduces the relative effective diffusivity in highly cracked MPLs. Heterogeneous distribution of reactant can result in current density gradients that can impact durability. This scenario is expected to be more representative of an operating PEMFC at low operating temperature and high RH ($T \approx 40 - 60$ °C, RH ≈ 1). At higher operating temperatures ($T \approx 70 - 90$ °C), the effect of phase-change of water must also be considered, and the presence of cracks can either reduce or increase the effective thermal conductivity depending on the amount of stored water [134,135]. Coupled mass and heat transport must be examined using a more elaborated two-phase model coupled with an electrochemistry model to assess the interplay between distributed water generation and phase change of water.

The results of the bimodal macropore electrode, featuring an average pore size of 9 μm with a patterned secondary phase of 17.5 μm, are shown in Fig. 6. As shown in Fig. 6(a), the in-plane permeability, K_{ip}, increases around one order of magnitude ($K_{ip} \approx 4 - 11 \times 10^{-12}$ m^2) when the secondary macropore fraction is increased ten-fold from nearly $\varepsilon_{\text{macro}} \approx 0.05$ up to $\varepsilon_{\text{macro}} \approx 0.55$. However, as stated by the Carman-Kozeny equation, permeability and specific surface area are inversely related to each other, since viscous friction is proportional to the flow wet area [42]. Consequently, as shown in Fig. 6(b), the permeability growth is accompanied by a reduction of the reactive specific surface area. The specific surface area of the examined electrode drops from $a \approx 0.14$ μm^{-1} at $\varepsilon_{\text{macro}} \approx 0.05$ to $a \approx 0.11$ μm^{-1} at $\varepsilon_{\text{macro}} \approx 0.55$. According to Eqs. (43a)–(43b), both the permeability and the specific surface area can be fitted to exponential functions of the form

$$K_{ip} = 3.95 \times 10^{-12} \exp\left(1.88\, \varepsilon_{\text{macro}}\right) \text{ m}^2 \quad R^2 = 0.99 \tag{43a}$$

$$a = 0.14 \exp\left(-0.37\, \varepsilon_{\text{macro}}\right) \text{ μm}^{-1} \qquad R^2 = 0.98 \tag{43b}$$

The relative effect of the secondary macropore fraction on permeability is stronger than that on specific surface area (i.e., higher exponential argument), given that $K_{ip} \sim R_f^2$ and $a \sim R_f^{-1}$ at equal porosity (as may be anticipated from dimensional analysis) [136]. The design of tailored macroporous electrodes with enhanced permeability and relatively high specific surface area has been shown in several experimental studies (see, e.g., [126,137] among others), and continues to be a source of research in combination with more advanced fabrication techniques, such as 3D printing [138]. The optimization of fibrous electrodes with bimodal pore sizes enables operation at higher velocity at virtually equal pumping loss, which in turn increases both Reynolds number and Sherwood number (mass transfer coefficient) for a fixed fiber radius [139,140] – see velocity distributions in Fig. 6(c). As a result, operation at higher peak power densities is possible, increasing the range of available charge/discharge rates of a battery. Alternatively, active area may be reduced for operation at intermediate power densities, leading to material saving [141]. Further work is still needed to optimize electrode and flow field coupling. The design of both components must be synergistic to ensure an appropriate flow distribution over the cell active area, so different electrodes can be optimal for a given flow field [142,143]. The best possible combination is still to be determined. State-of-the-art multimaterial, multiscale 3D printing can provide a versatile manufacturing technique to develop best theoretical designs [144].

Multiphysics and multiphase transport in CLs (and microporous electrodes) is challenging due to the small dimensions involved and the variety of coupled phenomena that take place. Transport in CLs has motivated a large body of experimental, numerical and theoretical work with the aim of understanding the effect of CL microstructure on PEMFC operation and optimizing this key porous
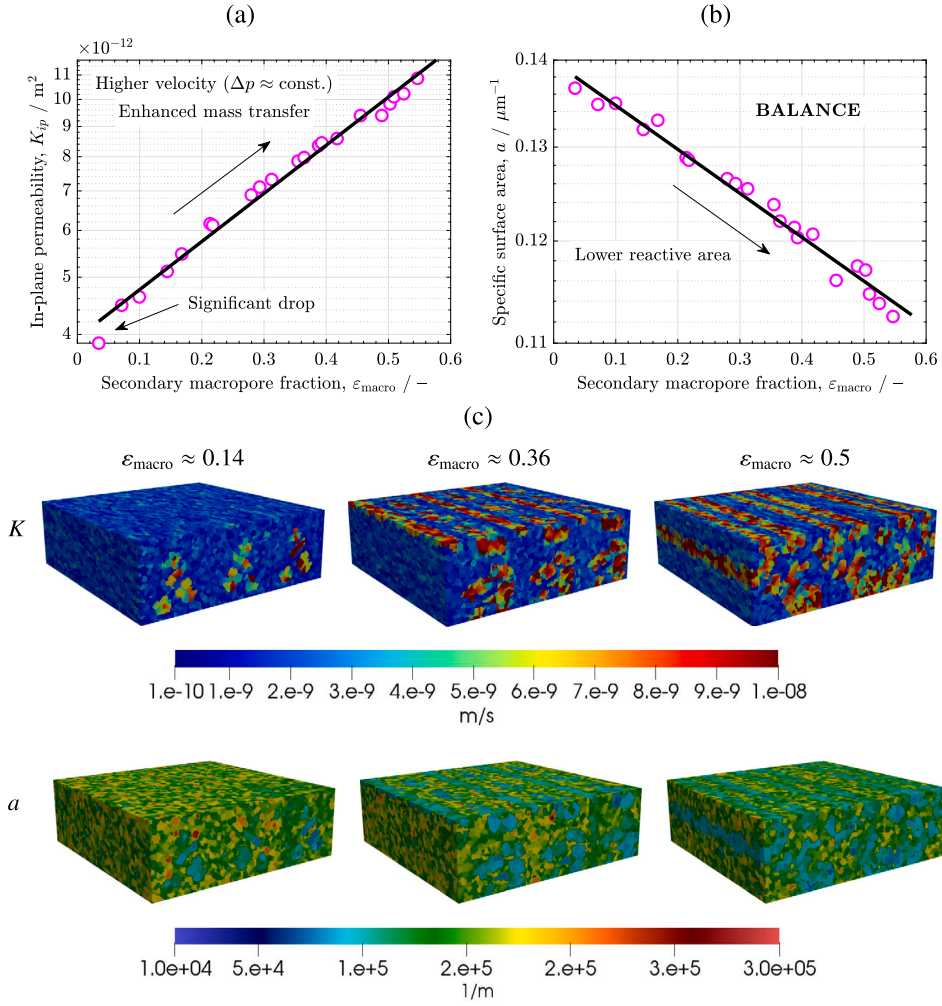
Fig. 6. Variation of (a) in-plane permeability, K_{ip}, and (b) specific surface area, a, as a function of secondary macropore volume fraction, $\varepsilon_{\text{macro}}$. (c) Distributions of velocity magnitude (top row) and specific surface area (bottom row), corresponding to permeability calculations at different $\varepsilon_{\text{macro}}$.

component (see, e.g., [14] and references therein). Fig. 7(a) shows the variation of the normalized dry effective diffusivity, $D_{\text{dry}}^{\text{eff}} D^{-1}$, with the electrode porosity, ε_{cl}, while Fig. 7(b) shows the variation of the effective (ionic) conductivity, $\sigma^{\text{eff}} \sigma^{-1}$, with the component volume fraction (i.e., ionomer volume fraction, $\varepsilon_k = \varepsilon_i$). Results for three different solid fractions are shown (curves with different markers and colors): $\varepsilon_{k,s} = 0.5$ ($\triangle$, red), $\varepsilon_{k,s} = 0.3$ ($\circ$, green), and $\varepsilon_{k,s} = 0.2$ ($\triangledown$, blue). According to Eqs. (44a)–(44b), the normalized effective diffusivity and the ionic conductivity are well correlated by power laws, showing good agreement with previous numerical and experimental data [145–149] (see corresponding distributions in Fig. 7(c))

$$\frac{D_{\text{dry}}^{\text{eff}}}{D} = 0.26 \left(\varepsilon_{cl} - 0.12 \right)^{1.55} \quad R^2 = 0.92 \tag{44a}$$

$$\frac{\sigma^{\text{eff}}}{\sigma} = 0.3 \varepsilon_i^{1.35} \qquad\qquad R^2 = 0.98 \tag{44b}$$

For a given ionomer volume fraction ($\varepsilon_k = \varepsilon_i$), a reduction of the solid fraction leads to a gradual decrease of the ionic conductivity, even though the effect is significantly lower than that of ε_i. The reduction is caused by the decreasing local volume fraction available for transport in the solid phase, which originates bottlenecks even if $\varepsilon_k = \varepsilon_i$ is the same. A qualitatively similar effect has been reported for the ionic conductivity of ionomer nanofilms due to the effect of substrate confinement and percolation [150–152]. It is worth noting that data in Fig. 7(a)-(b) are quite dispersed among authors. For effective diffusivity, variations can be mainly ascribed to Knudsen effect, so diffusion is hindered in CLs with a lower average pore radius due to frequent molecular collision with pore walls [11]. Other factors that can affect diffusivity variability are the fraction of macroporous cracks and defects [153], as well as the morphology arising from manufacturing (e.g., airbrushing vs. electrospraying [154]), aspects that have not been explicitly considered here. Less conclusive is the scenario found for the ionic conductivity, where values up to one order of magnitude higher than those shown in Fig. 7(b) were reported by Liu et al. [155]. These discrepancies in the ionic conductivity deserve a further analysis of
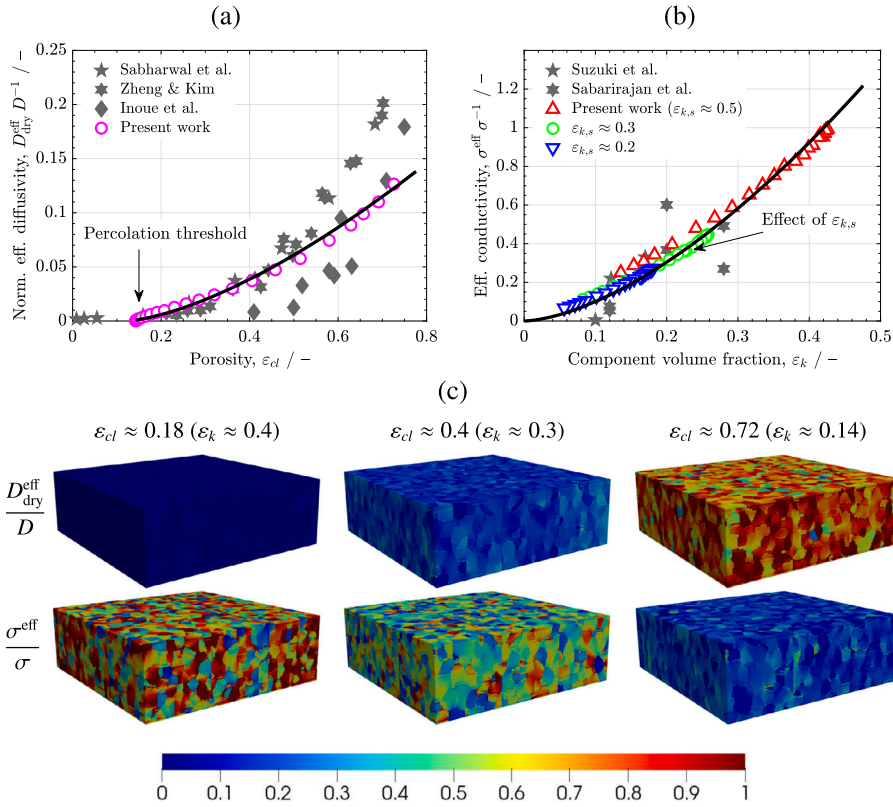
Fig. 7. Variation of (a) normalized dry effective diffusivity, $f = D_{\text{dry}}^{\text{eff}} D^{-1}$, as a function of electrode porosity, ε_{cl}, and (b) effective (ionic) conductivity, $\sigma^{\text{eff}} \sigma^{-1}$, as a function of solid component (ionomer) volume fraction, ε_k, for three different component volume fractions in the solid phase, $\varepsilon_{k,s}$. Results are compared with previous data: diffusivity [145–147] and ionic conductivity [148,149]. (c) Distributions of normalized through-plane diffusive and conductive flux, corresponding to dry diffusivity and conductivity calculations, respectively, at different ε and ε_k.

the multiscale ionomer network from the scale of a carbon particle up to the macroscopic scale, passing though the agglomerate scale. The impact of bottlenecks of thin ionomer films, the presence of thick ionomer highways and proton transport across flooded nanoregions must be delineated [14,156]. Understanding key factors that affect effective transport properties of CLs is crucial to ensure good manufacturing tolerances for large-scale commercialization.

The results of the membrane with graded humidification, i.e., varying RH at the bottom surface and well hydration at the top surface, are summarized in Fig. 8. A representative piece of material with a thickness of 200 nm was examined – larger heterogeneity can arise in state-of-the-art membranes around 10 μm thick. Mesoscopic diffusion and ionic conduction were modeled by Laplace equation, considering a non-linear self-diffusion coefficient of water, D_λ^{eff}, as typically observed in Nafion, and a water-dependent ionic conductivity, σ^{eff}, as given by the Nernst-Planck equation. Their expressions are given by Eqs. (45a)–(45b) [4,127,157,158]

$$D_\lambda^{\text{eff}} = A \left[1 + \tanh \left(\frac{\lambda - B}{C} \right) \right] \Upsilon_p \tag{45a}$$

$$\sigma^{\text{eff}} = \frac{\phi_w F^2 D_{\text{H}^+}^{\text{eff}} C_{\text{H}^+}}{\tau R^o T} \tag{45b}$$

where A, B and C are constants ($A = 4.1 \times 10^{-10}$ m^2 s^{-1}, $B = 2.2$, $C = 1.4$), λ is the water content in ionomer (i.e., water molecules per protogenic group), ϕ_w is the volume fraction of water, $D_{\text{H}^+}^{\text{eff}} \approx 9 \times 10^{-9}$ m^2 s^{-1} is the effective diffusion coefficient of protons, C_{H^+} is the proton concentration (in the fluid phase), τ is the tortuosity factor, Υ_p is the pore size coefficient, F is Faraday's constant, and T is the operating temperature (considered to be $T = 80$ °C). C_{H^+}, ϕ_w and τ are given by Eq. (46) [127,159]

$$C_{\text{H}^+} = \frac{\rho_{\text{dry}}(1 - \phi_w)}{EW \phi_w}; \quad \phi_w = \frac{\lambda M_w \tilde{\rho}}{\lambda M_w \tilde{\rho} + EW}; \quad \tau = A_\tau \left(\phi_w - \phi_w^{th} \right)^{-2}; \quad \tilde{\rho} = \frac{\rho_{\text{dry}}}{\rho_w} \tag{46}$$

where $A_\tau \approx 0.19$ S m^{-1}, $\phi_w^{th} \approx 0.02$ is the water percolation threshold, $\rho_{\text{dry}} \approx 1980$ kg m^{-1} (Nafion) and ρ_w are the dry density of ionomer and water, respectively, $EW \approx 1.1$ kg mol^{-1} (Nafion) is the equivalent weight, and M_w is the molecular mass of water.

According to Dorenbos and Suga [160], Υ_p decreases with increasing pore size due to the more tortuous pathways formed at higher intra- and inter-cluster distances. According to Eq. (47), Υ_p can be linearly correlated with the local fluid radius, R_f, as

$$\Upsilon_p = \max\left[1 + 0.4\left(\frac{R_p^{\mathrm{ref}} - R_f}{R_p^{\mathrm{ref}}}\right), 0\right] \tag{47}$$

where $R_p^{\mathrm{ref}} = 4$ nm is the reference pore size.

Introducing Kirchhoff's transformation, the linearized potential of water content, Θ_λ, and the backward Kirchhoff's transformation are given by Eqs. (48a)–(48b)

$$\Theta_\lambda = \int_0^\lambda D_\lambda^{\mathrm{eff}}(\eta)\,\mathrm{d}\eta = A\,C\log\left[\frac{\tanh\left(\frac{B}{C}\right) + 1}{\tanh\left(\frac{B-\lambda}{C}\right) + 1}\right] \tag{48a}$$

$$\lambda = B - C\operatorname{atanh}\left[\frac{\tanh\left(\frac{b}{c}\right) + 1}{\exp\left(\frac{\Theta_\lambda}{A\,C}\right)} - 1\right] \tag{48b}$$

where A, B and C are the coefficients in (45a).

At the bottom and top membrane surfaces, water content was assumed to be at thermodynamic equilibrium with the surrounding RH and water saturation, as given by the water sorption isotherm at the operating temperature T (see Eq. (49))

$$\lambda_{eq} = \begin{cases} \left[1 + 0.2352a^2\left(\frac{T - 303.15}{30}\right)\right]\left(14.22a^3 - 18.92a^2 + 13.41a\right) & a \leq 1 \\[2ex] \left[1 + 0.2352\left(\frac{T - 303.15}{30}\right)\right](8.71 + 3(a-1)) & a > 1 \end{cases} \tag{49}$$

where $a = \mathrm{RH} + 2s$ is the (effective) water activity.

As shown in Fig. 8(a) and Eq. (50a), the computed through-plane effective ionic conductivity, $\sigma_{tp}^{\mathrm{eff}}$, increases exponentially from around $4\,\mathrm{S\,m^{-1}}$ to $15\,\mathrm{S\,m^{-1}}$ as the bottom surface is gradually humidified (from $\mathrm{RH} = a = 0.1$ up to $\mathrm{RH} = 1$ ($s = 0.4$), $a = 1.8$)

$$\sigma_{tp}^{\mathrm{eff}} = 3.1\exp(1.6\,\mathrm{RH}) \quad R^2 = 0.99 \tag{50a}$$

The strong sensitivity of ionic conductivity to water arises from the bottleneck originated at the bottom surface, which is reduced as this surface is well hydrated. Graded water distributions in PEMFC membranes can be problematic due to dry-out of the anode side when a cell is operated with an oversaturated cathode and a dry anode at intermediate voltages [161,162]. Eventually, a cyclic response can be achieved if liquid water is periodically released from the cathode inlet, so that current density oscillates between low and high performance levels, as previously observed by García-Salaberri et al. [163]. In recent years, a growing effort has been devoted toward PEMFC operation at low humidification or even without any external humidification due to cost and weight reduction, and system simplification. However, operation at low humidification usually leads to a premature dry-out of the anode side, even if both flow fields are dry, because of water generation at the cathode and electro-osmotic drag. The design of membranes with increased water uniformity is not only necessary to increase average water content but to reduce local bottlenecks for proton conduction and heterogeneity, which can exacerbate membrane degradation. This aspect is emphasized in Fig. 8(b)–(c), which shows the variation of the homogeneity factor, HF, defined according to Eq. (50b)

$$\mathrm{HF} = 1 - \frac{\Delta j_y}{j_y^{\mathrm{avg}}} \tag{50b}$$

where $\Delta j_y = \max(j_y) - \min(j_y)$ is the amplitude of current density variation, and j_y^{avg} is the average current density. According to Eq. (50c), HF can be described through a logarithmic function, which passes through the point $(1, 1)$ (reference uniform condition)

$$\mathrm{HF} = 1 + \log(0.05\,\mathrm{RH}) \quad R^2 = 0.73 \tag{50c}$$

Water uniformity at low RH can be enhanced by increasing the number of adsorption points for water uptake and/or increasing the connectivity of water clusters. Strategies to accomplish this goal are the use of nanocracked membranes, membrane thinning and/or the incorporation of secondary porous phases, such as (doped) metal or covalent organic frameworks [164–167].

7. Limitations

The method introduced here is conceptually equivalent to PNM. The main difference arises in the description of pore network morphology, which is based on a tessellated CV decomposition in *POREnet*. Therefore, unlike PNM, the main limitation relies on the construction of a realistic tessellated representation of porous media space, which matches the coordination number and the spatial distribution of pores observed experimentally. This limitation can be mitigated by: (*i*) the combination of various tessellation algorithms rather than only Voronoi tessellation, and/or (*ii*) the extraction of tessellated CV networks from tomography images using algorithms based on watershed filtering. Another disadvantage is caused by the larger number of computational nodes needed to
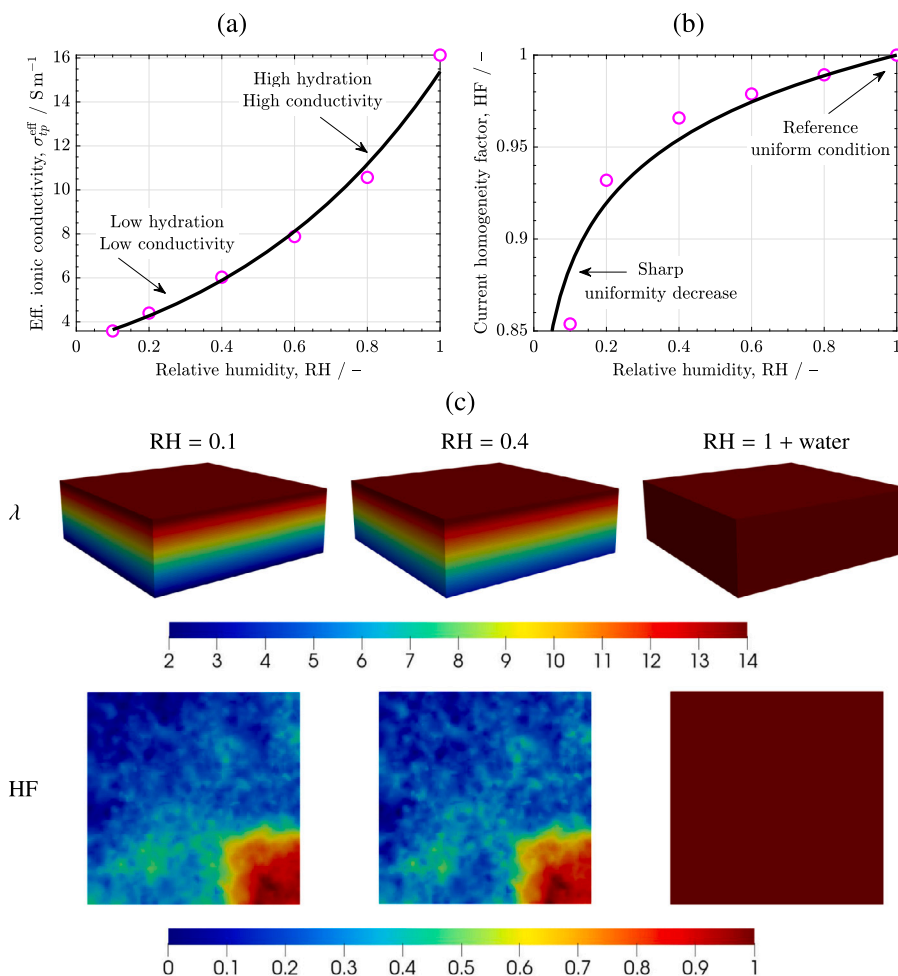
Fig. 8. Variation of (a) through-plane effective ionic conductivity, $\sigma_{tp}^{\text{eff}} \sigma^{-1}$, and (b) current density homogeneity factor, HF, as a function of RH at the bottom surface, RH. RH in the upper side is kept at fully humidified conditions with liquid water (RH = 1, s = 0.4). (c) Distributions of water content per protogenic group, λ, and normalized through-plane current density, corresponding to diffusivity and conductivity calculations, respectively, at different RH. HF = 1 is achieved when both sides of the electrolyte are well hydrated (RH = 1, s = 0.4).

describe heterogeneity, since several computational cells must be present in every tessellated CV. This drawback can be overcome thanks to the computational power of numerical schemes available in state-of-the-art CFD softwares. Further work is still needed to perform a one-to-one comparison against PNM and experimental data considering porous media with different morphologies (e.g., soils, rocks, fibrous materials, foams, etc.). The computational performance of using a continuum formulations must also be tested in supercomputing clusters.

In addition, it is worth noting that the present method relies on discrete algorithms to model IP under two-phase conditions despite the continuum formulation adopted for other transport processes. A fully continuum implementation may be achieved by incorporating microstructural information extracted from *POREnet* into a continuum two-phase formulation. For example, introducing local retention curves expressed in terms of local entry capillary pressure, and solving the heterogeneous partial differential equation for liquid saturation by means of Kirchhoff transformation.

8. Conclusions

Unlike pseudo-infinite domains in soils and rocks, thin porous media, TPM, are characterized by having a lateral dimension in the material plane much larger than their thickness. As a result, TPM present striking features which deserve special consideration, including but not limited to finite size, manufacturing defects and possibly a lack of separation between pore and layer scales. In this work, a novel general-purpose tool for extracting effective properties of multifunctional TPM, *POREnet*, has been presented. Effective transport properties implemented in *POREnet* are mass diffusivity, permeability, solid-phase conductivity (e.g., thermal conductivity or ionic conductivity), and entry capillary pressure and contact angle under two-phase conditions. Knudsen and slippage effects in nanoporous materials are also taken into account for diffusivity and permeability calculations, respectively. In addition, the code allows conductivity calculations of multi-component TPM with several solid phases and local contact resistances.

The method is built on a continuum tessellation of macroscopic porous regions using a Voronoi diagram (i.e., control volume, CV, assembly). Local effective property tensors are extracted from every Voronoi cell or polyhedron using a discretized dual pore network, PN, which is composed of a pore body and connecting throats, along with the surrounding solid space. Local effective transport properties are determined by volume averaging of the corresponding flux, normalized with respect to bulk transport in each Voronoi cell. 3D bulk fluxes are calculated thanks to the gradient theorem, which provides an appropriate metric for tessellated space with inlets/outlets. Unlike fully discrete PN methods, the calculation of local effective properties on a CV basis allows data saving in a continuum basis with 3D image stacks. As a result, interfacial and sub CV scale features can be added on 3D image stacks to reproduce layer-layer interfacial regions or manufacturing defects, such as high porosity in cracks. After post-processing, data can be exported to CFD meshes for simulation. The resulting modeling approach provides a versatile methodology for modeling multiphysics, multiphase and multiscale problems in conventional CFD codes, where a large variety of solution modules is available. In particular, the proposed method simplifies the analysis of transient problems and the coupling of discrete and continuum models using a single framework, as it is found when coupling a free-stream flow with a PN model at channel interfaces. Interfacial contact resistances can also be easily incorporated through robin boundary conditions.

The method was tested against a miscellaneousness of examples involving TPM from electrochemical applications: (*i*) gas species transport in a multiscale porous assembly (gas diffusion layer + microporous layer) under two-phase conditions; (*ii*) convective transport in macroporous electrodes with a bimodal pore size distribution; (*iii*) gas species transport and multi-component conduction in a nanoporous catalyst layer; and (*iv*) non-linear water transport and percolative ionic conduction in a membrane with a graded RH profile. These contrasting examples allowed us to check the correct functioning of *POREnet*, while discussing important aspects of transport in TPM and open questions to be addressed.

Several aspects warrant closer attention. Future work shall be devoted to: (*i*) generation of tessellated domains from tomography images using, e.g., watershed transform; (*ii*) implementation of other effective properties, such as mechanical properties based on composite material theory and Sherwood number based on generalized Lévêque equation; and (*iii*) optimization of the numerical code implemented in Matlab and speeding-up the code using faster, low-level programming languages (e.g., C++ or Julia). In tandem, the method should be tested not only to determine global effective properties, but to model multiphysics problems in a CFD software.

Nomenclature

Symbols

A	area / m^2
$\tilde{A}$	dimensionless area / –
AR	anisotropy ratio / –
a	specific surface area (also activity) / m^{-1} (–)
C	species concentration / mol m^{-3}
$\bar{C}$	centroid coordinate / m
C_a	capillary number / –
c	dimensionless shape factor or collision factor / –
c_F	Forchheimer constant / –
D	bulk mass diffusivity / mol m^{-2} s^{-1}
d	diameter / m
E	expected value / IS units
EW	ionomer equivalent weight / kg mol^{-1}
$\bar{e}_j$	unit Cartesian vector in j-direction (x, y, z) / –
F	slippage correction factor / –
f	normalized dry diffusivity (also Knudsen factor) / – (–)
G_m^j	conductance of transport mode m in j-direction / m^3 s^{-1} ($m = d$); m^3 ($m = h$); W K^{-1}, S ($m = s$)
g	relative effective diffusivity / –
HF	homogeneity factor / –
h	height / m
$\bar{J}$	scalar transport flux / IS units
$\bar{j}$	diffusive, conductive flux / mol m^{-2} s^{-1}, W m^{-2}, A m^{-2}
K	absolute permeability / m^2
K_{ck}	Carman-Kozeny constant / –
k_o	permeability shape factor / –
L	length / m
L_{cv}^{ij}	control volume metric / m
l	longitudinal coordinate / m
$\bar{\ell}$	unit longitudinal vector / –
M	molecular mass / kg mol^{-1}
N_i	number of element i / –
$\bar{n}$	outward unit normal vector / –

$\bar{P}$	spatial position vector (point) / m
p	pressure / Pa
p_e	entry pressure / Pa
R	radius / m
R^o	universal gas constant / $J\,K^{-1}\,mol^{-1}$
S	bulk solid-phase thermal, electrical conductivity / $W\,m^{-1}\,K^{-1}$, $S\,m^{-1}$
S_p	downscaling factor / –
s	solid-phase scalar, e.g., temperature, voltage (also saturation) (also apothem) / K, V (–) (m)
T	temperature / K
$\bar{u}$	velocity vector / $m\,s^{-1}$
V	volume / m^3
x	primary in-plane coordinate / m
y	through-plane coordinate / m
z	secondary in-plane coordinate / m

Greek letters

α_i	pore/throat isotropic scaling parameter / –
$\bar{\beta}$	pore/throat directional scaling parameter / –
Γ_{ij}	dimensionless parameter tensor / –
γ	angle beyond the apex of a curved throat (also apex semi-angle in Fig. 3) / –
δ	extended distance of "background PM" around modeling domain / m
ε_i	volume fraction per unit total volume of phase/component i / –
η	integration variable (Kirchhoff's transformation) / IS units
Θ	linearized potential (Kirchhoff's transformation) / IS units
θ	contact angle / –
λ	mean free path (also ionomer water content) / m (–)
μ	dynamic viscosity / $kg\,m^{-1}\,s^{-1}$
Π	scalar transport diffusivity / IS units
π	transport scalar / IS units
ρ	density / $kg\,m^{-3}$
σ	surface tension (also ionic conductivity) / $N\,m^{-1}$ ($S\,m^{-1}$)
τ_m^{ij}	tortuosity tensor of transport mode m / –
Υ	pore size coefficient / –
ϕ	water volume fraction in ionomer / –
χ_m^j	partition coefficient of transport mode m in j-direction / –

Subscripts and superscripts

avg	average
b	base
bulk	bulk property
c	capillary
cfd	computational fluid dynamics
cl	catalyst layer
cv	control volume
d	diffusive
dry	dry condition
eff	effective
eq	equivalent
f	fluid
fcv	control volume face
fpb	pore body face
g	gas
gdl	gas diffusion layer
gen	generation
h	hydraulic
i	i-direction
ij	tensor indices
in	inlet
int	interfacial
ip	in-plane direction
j	j-direction

kn	Knudsen
l	liquid
max	maximum
min	minimum
mpl	microporous layer
ns	solid node ($ns = 1, \ldots, N_t$)
o	outlet
p	pore
ps	solid pair in solid node ns ($ps = 1, \ldots, N_{ps}$)
ref	reference
s	solid phase
t	fluid throat ($t = 1, \ldots, N_t$)
th	threshold
tp	through-plane direction
w	water
wet	wet condition

CRediT authorship contribution statement

Pablo A. García-Salaberri: Conceptualization, Data curation, Formal analysis, Funding acquisition, Investigation, Methodology, Project administration, Resources, Software, Supervision, Validation, Visualization, Writing – original draft, Writing – review & editing. **Iryna V. Zenyuk:** Formal analysis, Investigation, Writing – original draft, Writing – review & editing.

Declaration of competing interest

The authors declare that they have no known competing financial interests or personal relationships that could have appeared to influence the work reported in this paper.

Acknowledgements

References

[1] Marc Prat, Tristan Agaësse, Thin Porous Media, Handbook of Porous Media, 2015, pp. 89–112.

[2] Pablo A. García-Salaberri, Iryna V. Zenyuk, Andrew D. Shum, Gisuk Hwang, Marcos Vera, Adam Z. Weber, Jeff T. Gostick, Analysis of representative elementary volume and through-plane regional characteristics of carbon-fiber papers: diffusivity, permeability and electrical/thermal conductivity, Int. J. Heat Mass Transf. 127 (2018) 687–703.

[3] Jennifer Hack, Pablo A. García-Salaberri, Matthew D.R. Kok, Rhodri Jervis, Paul R. Shearing, Nigel Brandon, Dan J.L. Brett, X-ray micro-computed tomography of polymer electrolyte fuel cells: what is the representative elementary area?, J. Electrochem. Soc. 167 (1) (2020) 013545.

[4] Nieves Ureña, M. Teresa Pérez-Prior, Belén Levenfeld, Pablo A. García-Salaberri, On the conductivity of proton-exchange membranes based on multiblock copolymers of sulfonated polysulfone and polyphenylsulfone: an experimental and modeling study, Polymers 13 (3) (2021) 363.

[5] Pablo A. García-Salaberri, General aspects in the modeling of fuel cells: from conventional fuel cells to nano fuel cells, in: Nanotechnology in Fuel Cells, Elsevier, 2022, pp. 77–121.

[6] Marc Secanell, Jeff Gostick, Pablo A. Garcia-Salaberri, Porous electrode components in polymer electrolyte fuel cells and electrolyzers, in: Luisa F. Cabeza (Ed.), Encyclopedia of Energy Storage, Elsevier, Oxford, 2022, pp. 290–298.

[7] Pablo A. García-Salaberri, Marcos Vera, Ramon Zaera, Nonlinear orthotropic model of the inhomogeneous assembly compression of pem fuel cell gas diffusion layers, Int. J. Hydrog. Energy 36 (18) (2011) 11856–11870.

[8] Pablo A. García-Salaberri, Marcos Vera, On the effect of operating conditions in liquid-feed direct methanol fuel cells: a multiphysics modeling approach, Energy 113 (2016) 1265–1287.

[9] Pablo A. García-Salaberri, Gisuk Hwang, Marcos Vera, Adam Z. Weber, Jeff T. Gostick, Effective diffusivity in partially-saturated carbon-fiber gas diffusion layers: effect of through-plane saturation distribution, Int. J. Heat Mass Transf. 86 (2015) 319–333.

[10] P.A. García-Salaberri, Modeling diffusion and convection in thin porous transport layers using a composite continuum-network model: application to gas diffusion layers in polymer electrolyte fuel cells, Int. J. Heat Mass Transf. 167 (2021) 120824.

[11] Arturo Sánchez-Ramos, Jeff T. Gostick, Pablo A. García-Salaberri, Modeling the effect of low pt loading cathode catalyst layer in polymer electrolyte fuel cells. Part i: model formulation and validation, J. Electrochem. Soc. 168 (12) (2021) 124514.

[12] Arturo Sánchez-Ramos, Jeff T. Gostick, Pablo A. García-Salaberri, Modeling the effect of low pt loading cathode catalyst layer in polymer electrolyte fuel cells. Part ii: parametric analysis, J. Electrochem. Soc. 169 (7) (2022) 074503.

[13] Vanesa Muñoz-Perales, Sabrina Berling, Enrique García-Quismondo, Pablo A. García-Salaberri, Jesús Palma, Marcos Vera, Santiago E. Ibáñez, Investigating the effects of operation variables on all-vanadium redox flow batteries through an advanced unit-cell model, J. Electrochem. Soc. 169 (10) (2022) 100522.

[14] Pablo A. García-Salaberri, Arturo Sánchez-Ramos, Prodip K. Das, On the optimal cathode catalyst layer for polymer electrolyte fuel cells: bimodal pore size distributions with functionalized microstructures, Front. Energy Res. (2022).

[15] Pablo A. García-Salaberri, Tugba Ceren Gokoglan, Santiago E. Ibáñez, Ertan Agar, Marcos Vera, Modeling the effect of channel tapering on the pressure drop and flow distribution characteristics of interdigitated flow fields in redox flow batteries, Processes 8 (7) (2020) 775.

[16] Diego Zapardiel, Pablo A. García-Salaberri, Modeling the interplay between water capillary transport and species diffusion in gas diffusion layers of proton exchange fuel cells using a hybrid computational fluid dynamics formulation, J. Power Sources 520 (2022) 230735.

[17] Pablo A. García-Salaberri, Iryna V. Zenyuk, Gisuk Hwang, Marcos Vera, Adam Z. Weber, Jeff T. Gostick, Implications of inherent inhomogeneities in thin carbon fiber-based gas diffusion layers: a comparative modeling study, Electrochim. Acta 295 (2019) 861–874.

[18] Lilit Yeghiazarian, Krishna Pillai, Rodrigo Rosati, Thin porous media, Transp. Porous Media 115 (2016) 407–410.

[19] Yehuda Bachmat, Jacob Bear, On the concept and size of a representative elementary volume (rev), in: Advances in Transport Phenomena in Porous Media, 1987, pp. 3–20.

[20] Yehuda Bachmat, Jacob Bear, Macroscopic modelling of transport phenomena in porous media. 1: the continuum approach, Transp. Porous Media 1 (1986) 213–240.

[21] Rebai Mehdi, Marc Prat, Scale effect and two-phase flow in a thin hydrophobic porous layer. Application to water transport in gas diffusion layers of proton exchange membrane fuel cells, J. Power Sources 192 (2) (2009) 534–543.

[22] C.Z. Qin, S.M. Hassanizadeh, Multiphase flow through multilayers of thin porous media: general balance equations and constitutive relationships for a solid–gas–liquid three-phase system, Int. J. Heat Mass Transf. 70 (2014) 693–708.

[23] Pablo A. García-Salaberri, Jeff T. Gostick, Iryna V. Zenyuk, Gisuk Hwang, Marcos Vera, Adam Z. Weber, On the limitations of volume-averaged descriptions of gas diffusion layers in the modeling of polymer electrolyte fuel cells, ECS Trans. 80 (8) (2017) 133.

[24] Adam Z. Weber, Rodney L. Borup, Robert M. Darling, Prodip K. Das, Thomas J. Dursch, Wenbin Gu, David Harvey, Ahmet Kusoglu, Shawn Litster, Matthew M. Mench, et al., A critical review of modeling transport phenomena in polymer-electrolyte fuel cells, J. Electrochem. Soc. 161 (12) (2014) F1254.

[25] M. Sabharwal, L.M. Pant, A. Putz, D. Susac, J. Jankovic, M. Secanell, Analysis of catalyst layer microstructures: from imaging to performance, Fuel Cells 16 (6) (2016) 734–753.

[26] Mohammad Ahadi, Heat and electron conduction in microporous catalyst layers of polymer electrolyte membrane fuel cells, 2018.

[27] J.O. Ceballos, L.C. Ordoñez, J.M. Sierra, Numerical simulation of a pem fuel cell: effect of tortuosity parameters on the construction of polarization curves, Int. J. Hydrog. Energy 47 (70) (2022) 30291–30302.

[28] Li Chen, Ya-Ling He, Qinjun Kang, Wen-Quan Tao, Coupled numerical approach combining finite volume and lattice Boltzmann methods for multi-scale multi-physicochemical processes, J. Comput. Phys. 255 (2013) 83–105.

[29] Oladapo Christopher Esan, Xingyi Shi, Zhefei Pan, Xiaoyu Huo, Liang An, T.S. Zhao, Modeling and simulation of flow batteries, Adv. Energy Mater. 10 (31) (2020) 2000758.

[30] Pablo A. García-Salaberri, Effect of thickness and outlet area fraction of macroporous gas diffusion layers on oxygen transport resistance in water injection simulations, Transp. Porous Media 145 (2) (2022) 413–440.

[31] Iryna V. Zenyuk, Ezequiel Medici, Jeffrey Allen, Adam Z. Weber, Coupling continuum and pore-network models for polymer-electrolyte fuel cells, Int. J. Hydrog. Energy 40 (46) (2015) 16831–16845.

[32] Mahmoudreza Aghighi, Michael A. Hoeh, Werner Lehnert, Geraldine Merle, Jeff Gostick, Simulation of a full fuel cell membrane electrode assembly using pore network modeling, J. Electrochem. Soc. 163 (5) (2016) F384.

[33] Najib Belgacem, Marc Prat, Joel Pauchet, Coupled continuum and condensation–evaporation pore network model of the cathode in polymer-electrolyte fuel cell, Int. J. Hydrog. Energy 42 (12) (2017) 8150–8165.

[34] Kilian Weishaupt, Vahid Joekar-Niasar, Rainer Helmig, An efficient coupling of free flow and porous media flow using the pore-network modeling approach, J. Comput. Phys. X 1 (2019) 100011.

[35] Sina Ackermann, Carina Bringedal, Rainer Helmig, Multi-scale three-domain approach for coupling free flow and flow in porous media including droplet-related interface processes, J. Comput. Phys. 429 (2021) 109993.

[36] S. Succi, E. Foti, F. Higuera, Three-dimensional flows in complex geometries with the lattice Boltzmann method, Europhys. Lett. 10 (5) (1989) 433.

[37] Amir H. Kohanpur, Yu Chen, Albert J. Valocchi, Using direct numerical simulation of pore-level events to improve pore-network models for prediction of residual trapping of CO_2, Front. Water 3 (2022) 710160.

[38] Mosayeb Shams, Kamaljit Singh, Branko Bijeljic, Martin J. Blunt, Direct numerical simulation of pore-scale trapping events during capillary-dominated two-phase flow in porous media, Transp. Porous Media 138 (2) (2021) 443–458.

[39] Hyoung Suk Suh, Tae Sup Yun, Modification of capillary pressure by considering pore throat geometry with the effects of particle shape and packing features on water retention curves for uniformly graded sands, Comput. Geotech. 95 (2018) 129–136.

[40] Irving Fatt, The network model of porous media, Trans. AIME 207 (01) (1956) 144–181.

[41] Josef Kozeny, Über kapillare Leitung des Wassers im Boden-Aufstieg, Versickerung und Anwendung auf die Bewässerung, Sitzungsber. Akad. Wiss. Wien, Math.-Naturwiss. Abt. 136 (1927) 271–306.

[42] P.C. Carman, Fluid flow through granular beds, Chem. Eng. Res. Des. 75 (1997) S32–S48.

[43] Francis AL Dullien, New network permeability model of porous media, AIChE J. 21 (2) (1975) 299–307.

[44] Ioannis Chatzis, Francis AL Dullien, Modelling pore structure by 2-d and 3-d networks with applicationto sandstones, J. Can. Pet. Technol. 16 (01) (1977).

[45] David Wilkinson, Jorge F. Willemsen, Invasion percolation: a new form of percolation theory, J. Phys. A, Math. Gen. 16 (14) (1983) 3365.

[46] Marc Prat, Percolation model of drying under isothermal conditions in porous media, Int. J. Multiph. Flow 19 (4) (1993) 691–704.

[47] Marc Prat, Recent advances in pore-scale models for drying of porous media, Chem. Eng. J. 86 (1–2) (2002) 153–164.

[48] Martin J. Blunt, Flow in porous media—pore-network models and multiphase flow, Curr. Opin. Colloid Interface Sci. 6 (3) (2001) 197–207.

[49] Martin Blunt, Peter King, Relative permeabilities from two- and three-dimensional pore-scale network modelling, Transp. Porous Media 6 (1991) 407–433.

[50] Hooshang Kharabaf, Yanis C. Yortsos, Pore network model for foam formation and propagation in porous media, SPE J. 3 (01) (1998) 42–53.

[51] F. Thauvin, K.K. Mohanty, Network modeling of non-Darcy flow through porous media, Transp. Porous Media 31 (1) (1998) 19–37.

[52] D.S. Freitas, Marc Prat, Pore network simulation of evaporation of a binary liquid from a capillary porous medium, Transp. Porous Media 40 (2000) 1–25.

[53] V. Joekar-Niasar, S.M. Hassanizadeh, Analysis of fundamentals of two-phase flow in porous media using dynamic pore-network models: a review, Crit. Rev. Environ. Sci. Technol. 42 (18) (2012) 1895–1976.

[54] Younes Amini, Javad Karimi-Sabet, Mohsen Nasr Esfahany, Experimental and numerical simulation of dry pressure drop in high-capacity structured packings, Chem. Eng. Technol. 39 (6) (2016) 1161–1170.

[55] Younes Amini, Mohsen Nasr Esfahany, Cfd simulation of the structured packings: a review, Sep. Sci. Technol. 54 (15) (2019) 2536–2554.

[56] Antonio Rodríguez de Castro, Benoit Goyeau, A pore network modelling approach to investigate the interplay between local and Darcy viscosities during the flow of shear-thinning fluids in porous media, J. Colloid Interface Sci. 590 (2021) 446–457.

[57] Maša Prodanović, Ayaz Mehmani, Adrian P. Sheppard, Imaged-based multiscale network modelling of microporosity in carbonates, Geol. Soc. (Lond.) Spec. Publ. 406 (1) (2015) 95–113.

[58] Na Zhang, Yating Wang, Qian Sun, Yuhe Wang, Multiscale mass transfer coupling of triple-continuum and discrete fractures for flow simulation in fractured vuggy porous media, Int. J. Heat Mass Transf. 116 (2018) 484–495.

[59] Mohammad Amin Sadeghi, Mahmoudreza Aghighi, Jake Barralet, Jeff T. Gostick, Pore network modeling of reaction-diffusion in hierarchical porous particles: the effects of microstructure, Chem. Eng. J. 330 (2017) 1002–1011.

[60] Zohaib Atiq Khan, Pablo Angel Garcia Salaberri, Thomas M.M. Heenan, Rhodri Jervis, Paul R. Shearing, Dan Brett, Ali Elkamel, Jeff T. Gostick, Probing the structure-performance relationship of lithium-ion battery cathodes using pore-networks extracted from three-phase tomograms, J. Electrochem. Soc. 167 (4) (2020) 040528.

[61] Zeyun Jiang, M.I.J. Van Dijke, Kenneth Stuart Sorbie, Gary Douglas Couples, Representation of multiscale heterogeneity via multiscale pore networks, Water Resour. Res. 49 (9) (2013) 5437–5449.

[62] D. Bauer, S. Youssef, M. Han, S. Bekri, E. Rosenberg, M. Fleury, O. Vizika, From computed microtomography images to resistivity index calculations of heterogeneous carbonates using a dual-porosity pore-network approach: influence of percolation on the electrical transport properties, Phys. Rev. E 84 (1) (2011) 011133.

[63] Jacques Fize, Gaurav Shrivastava, Pierre André Ménard, Geodict: an integrated gazetteer, in: Proceedings of Language, Ontology, Terminology and Knowledge Structures Workshop (LOTKS 2017), 2017.

[64] D. Niblett, M. Mamlouk, O. Emmanuel Godinez Brizuela, Porous Microstructure Generator, Newcastle University, 2022, software.

[65] Zohaib Atiq Khan, Tom Tranter, Mehrez Agnaou, Ali Elkamel, Jeff Gostick, Dual network extraction algorithm to investigate multiple transport processes in porous materials: image-based modeling of pore and grain scale processes, Comput. Chem. Eng. 123 (2019) 64–77.

[66] X. Yu, C. Hong, G. Peng, S. Lu, Response of pore structures to long-term fertilization by a combination of synchrotron radiation X-ray microcomputed tomography and a pore network model, Eur. J. Soil Sci. 69 (2) (2018) 290–302.

[67] Jiangjin Liu, Pablo A. García-Salaberri, Iryna V. Zenyuk, Bridging scales to model reactive diffusive transport in porous media, J. Electrochem. Soc. 167 (1) (2019) 013524.

[68] Jiangjin Liu, Pablo A. García-Salaberri, Iryna V. Zenyuk, The impact of reaction on the effective properties of multiscale catalytic porous media: a case of polymer electrolyte fuel cells, Transp. Porous Media 128 (2019) 363–384.

[69] Cynthia Michalkowski, Maziar Veyskarami, Carina Bringedal, Rainer Helmig, Veronika Schleper, Two-phase flow dynamics at the interface between gdl and gas distributor channel using a pore-network model, Transp. Porous Media 144 (2) (2022) 429–458.

[70] K. Baber, B. Flemisch, R. Helmig, Modeling drop dynamics at the interface between free and porous-medium flow using the mortar method, Int. J. Heat Mass Transf. 99 (2016) 660–671.

[71] Xiang Lu, Evangelos Tsotsas, Abdolreza Kharaghani, Drying of capillary porous media simulated by coupling of continuum-scale and micro-scale models, Int. J. Multiph. Flow 140 (2021) 103654.

[72] Matthew T. Balhoff, Karsten E. Thompson, Martin Hjortsø, Coupling pore-scale networks to continuum-scale models of porous media, Comput. Geosci. 33 (3) (2007) 393–410.

[73] Matthew T. Balhoff, Sunil G. Thomas, Mary F. Wheeler, Mortar coupling and upscaling of pore-scale models, Comput. Geosci. 12 (2008) 15–27.

[74] Tie Sun, Yashar Mehmani, Jaideep Bhagmane, Matthew Thomas Balhoff, Pore to continuum upscaling of permeability in heterogeneous porous media using mortars, Int. J. Oil Gas Coal Technol. 5 (2–3) (2012) 249–266.

[75] Jay Chu, Björn Engquist, Maša Prodanović, Richard Tsai, A multiscale method coupling network and continuum models in porous media i: steady-state single phase flow, Multiscale Model. Simul. 10 (2) (2012) 515–549.

[76] Jeff Gostick, Mahmoudreza Aghighi, James Hinebaugh, Tom Tranter, Michael A. Hoeh, Harold Day, Brennan Spellacy, Mostafa H. Sharqawy, Aimy Bazylak, Alan Burns, et al., Openpnm: a pore network modeling package, Comput. Sci. Eng. 18 (4) (2016) 60–74.

[77] J. Zhou, A. Putz, M. Secanell, A mixed wettability pore size distribution based mathematical model for analyzing two-phase flow in porous electrodes, J. Electrochem. Soc. 164 (6) (2017) F530.

[78] Adam Z. Weber, Improved modeling and understanding of diffusion-media wettability on polymer-electrolyte-fuel-cell performance, J. Power Sources 195 (16) (2010) 5292–5304.

[79] Michael D. Hirschhorn, D.C. Hunt, Equilateral convex pentagons which tile the plane, J. Comb. Theory, Ser. A 39 (1) (1985) 1–18.

[80] Margaret S. Mackisack, Roger E. Miles, Homogeneous rectangular tessellations, Adv. Appl. Probab. 28 (4) (1996) 993–1013.

[81] J. Sadoc, Amorphous structural models using regular tessellation of curved spaces, J. Phys. Colloq. 41 (1980) C8.

[82] John H. Conway, Yang Jiao, Salvatore Torquato, New family of tilings of three-dimensional Euclidean space by tetrahedra and octahedra, Proc. Natl. Acad. Sci. 108 (27) (2011) 11009–11012.

[83] Cameron Talischi, Glaucio H. Paulino, Anderson Pereira, Ivan F.M. Menezes, Polymesher: a general-purpose mesh generator for polygonal elements written in Matlab, Struct. Multidiscip. Optim. 45 (2012) 309–328.

[84] Zohaib Atiq Khan, Ali Elkamel, Jeff T. Gostick, Efficient extraction of pore networks from massive tomograms via geometric domain decomposition, Adv. Water Resour. 145 (2020) 103734.

[85] Maxime van der Heijden, Rik van Gorp, Mohammad Amin Sadeghi, Jeffrey Gostick, Antoni Forner-Cuenca, Assessing the versatility and robustness of pore network modeling to simulate redox flow battery electrode performance, J. Electrochem. Soc. 169 (4) (2022) 040505.

[86] John D'Errico, Inhull, Matlab central file exchange, 2023.

[87] Tianyu Fu, Federico Monaco, Jizhou Li, Kai Zhang, Qingxi Yuan, Peter Cloetens, Piero Pianetta, Yijin Liu, Deep-learning-enabled crack detection and analysis in commercial lithium-ion battery cathodes, Adv. Funct. Mater. 32 (39) (2022) 2203070.

[88] Yadvinder Singh, Robin T. White, Marina Najm, Tylynn Haddow, Vivian Pan, Francesco P. Orfino, Monica Dutta, Erik Kjeang, Tracking the evolution of mechanical degradation in fuel cell membranes using 4d in situ visualization, J. Power Sources 412 (2019) 224–237.

[89] Jeff T. Gostick, Random pore network modeling of fibrous pemfc gas diffusion media using Voronoi and Delaunay tessellations, J. Electrochem. Soc. 160 (8) (2013) F731.

[90] Pablo A. García-Salaberri, Jeff T. Gostick, Gisuk Hwang, Adam Z. Weber, Marcos Vera, Effective diffusivity in partially-saturated carbon-fiber gas diffusion layers: effect of local saturation and application to macroscopic continuum models, J. Power Sources 296 (2015) 440–453.

[91] Jaka Dujc, Antoni Forner-Cuenca, Philip Marmet, Magali Cochet, Roman Vetter, Jürgen O. Schumacher, Pierre Boillat, Modeling the effects of using gas diffusion layers with patterned wettability for advanced water management in proton exchange membrane fuel cells, Adv. Electrochem. Energy Convers. Storage 15 (2) (2018).

[92] Heng Zhang, Lijun Zhu, Hesam Bazargan Harandi, Kangjun Duan, Roswitha Zeis, Pang-Chieh Sui, Po-Ya Abel Chuang, Microstructure reconstruction of the gas diffusion layer and analyses of the anisotropic transport properties, Energy Convers. Manag. 241 (2021) 114293.

[93] M.F. Mathias, Joerg Roth, Jerry Fleming, Werner Lehnert, Diffusion media materials and characterisation, in: Handbook of Fuel Cells—Fundamentals, Technology and Applications, 2003, pp. 517–537, 3(Part 1).

[94] T.G. Tranter, J.T. Gostick, A.D. Burns, W.F. Gale, Capillary hysteresis in neutrally wettable fibrous media: a pore network study of a fuel cell electrode, Transp. Porous Media 121 (2018) 597–620.

[95] Thomas G. Tranter, P. Boillat, A. Mularczyk, V. Manzi-Orezzoli, P.R. Shearing, D.J.L. Brett, J. Eller, J.T. Gostick, A. Forner-Cuenca, Pore network modelling of capillary transport and relative diffusivity in gas diffusion layers with patterned wettability, J. Electrochem. Soc. 167 (11) (2020) 114512.

[96] E.C. Kumbur, K.V. Sharp, M.M. Mench, Liquid droplet behavior and instability in a polymer electrolyte fuel cell flow channel, J. Power Sources 161 (1) (2006) 333–345.

[97] Christopher P. Liu, Prantik Saha, Ying Huang, Sirivatch Shimpalee, Pongsarun Satjaritanun, Iryna V. Zenyuk, Measurement of contact angles at carbon fiber–water–air triple-phase boundaries inside gas diffusion layers using X-ray computed tomography, ACS Appl. Mater. Interfaces 13 (17) (2021) 20002–20013.

[98] Mohammad Javad Shojaei, Branko Bijeljic, Yihuai Zhang, Martin J. Blunt, Minimal surfaces in porous materials: X-ray image-based measurement of the contact angle and curvature in gas diffusion layers to design optimal performance of fuel cells, ACS Appl. Energy Mater. 5 (4) (2022) 4613–4621.

[99] Daniel Niblett, Vahid J. Niasar, Adrian Mularczyk, Jens Eller, Stuart Holmes, Pore-Scale Performance Analysis of Ordered Microstructures as Gas Diffusion Layers in Fuel Cells, In Electrochemical Society Meeting Abstracts 237, vol. 38, The Electrochemical Society, Inc., 2020, p. 1610.

[100] Hongyan Song, Yu-Ting Liu, Xiao-Fang Zhang, Wei-Song Zhang, Gang-Ping Wu, Bimodal effect on mass transport of proton exchange membrane fuel cells by regulating the content of whisker-like carbon nanotubes in microporous layer, J. Power Sources 560 (2023) 232714.

[101] M.I.J. Van Dijke, S.R. McDougall, K.S. Sorbie, Three-phase capillary pressure and relative permeability relationships in mixed-wet systems, Transp. Porous Media 44 (2001) 1–32.
[102] V. Mani, K.K. Mohanty, Effect of the spreading coefficient on three-phase flow in porous media, J. Colloid Interface Sci. 187 (1) (1997) 45–56.
[103] R.M.S. Gama, R. Pazetto, S. Gama, The Kirchhoff transformation and the Fick's second law with concentration-dependent diffusion coefficient, WSEAS Trans. Heat Mass Transf. 16 (2021) 59–67.
[104] Peter Vadasz, Analytical solution to nonlinear thermal diffusion: Kirchhoff versus Cole–Hopf transformations, J. Heat Transf. 132 (12) (2010).
[105] Heejun Suk, Eungyu Park, Numerical solution of the Kirchhoff-transformed Richards equation for simulating variably saturated flow in heterogeneous layered porous media, J. Hydrol. 579 (2019) 124213.
[106] Saul A. Teukolsky, Brian P. Flannery, W.H. Press, W.T. Vetterling, Numerical recipes in C, SMR 693 (1) (1992) 59–70.
[107] F.M.S. Lima, Using surface integrals for checking Archimedes' law of buoyancy, Eur. J. Phys. 33 (1) (2011) 101.
[108] Frank M. White, Fluid Mechanics, Mcgraw-Hill, New York, 1994.
[109] Immaculada Iglesias Estradé, Carlos Martinez Bazán, Antonio Luis Sánchez Pérez, Marcos Vera Coello, Ingeniería fluidomecánica, Ediciones Paraninfo, SA, 2012.
[110] Sen Wang, Qihong Feng, Farzam Javadpour, Ming Zha, Ronghao Cui, Multiscale modeling of gas transport in shale matrix: an integrated study of molecular dynamics and rigid-pore-network model, SPE J. 25 (03) (2020) 1416–1442.
[111] Arash Rabbani, Masoud Babaei, Hybrid pore-network and lattice-Boltzmann permeability modelling accelerated by machine learning, Adv. Water Resour. 126 (2019) 116–128.
[112] Niloo Misaghian, Mehrez Agnaou, Mohammad Amin Sadeghi, Hamed Fathiannasab, Isma Hadji, Edward Roberts, Jeff Gostick, Prediction of diffusional conductance in extracted pore network models using convolutional neural networks, Comput. Geosci. 162 (2022) 105086.
[113] Wonjin Yun, Yimin Liu, Anthony R. Kovscek, Deep learning for automated characterization of pore-scale wettability, Adv. Water Resour. 144 (2020) 103708.
[114] Deqiang Mu, Zhong-Sheng Liu, Cheng Huang, Ned Djilali, Determination of the effective diffusion coefficient in porous media including Knudsen effects, Microfluid. Nanofluid. 4 (2008) 257–260.
[115] Boguslaw Kruczek, Carman–Kozeny Equation, Springer Berlin Heidelberg, Berlin, Heidelberg, 2015, pp. 1–3.
[116] Artur Duda, Zbigniew Koza, Maciej Matyka, Hydraulic tortuosity in arbitrary porous media flow, Phys. Rev. E 84 (3) (2011) 036319.
[117] Matyka Maciej, Zbigniew Koza, How to Calculate Tortuosity Easily?, AIP Conference Proceedings 4, vol. 1453, American Institute of Physics, 2012, pp. 17–22.
[118] Gordon P. Brown, Albert DiNardo, George K. Cheng, Thomas K. Sherwood, The flow of gases in pipes at low pressures, J. Appl. Phys. 17 (10) (1946) 802–813.
[119] Pengwei Zhang, Liming Hu, Jay N. Meegoda, Shengyan Gao, Micro/nano-pore network analysis of gas flow in shale matrix, Sci. Rep. 5 (1) (2015) 13501.
[120] Donald A. Nield, Adrian Bejan, et al., Convection in Porous Media, vol. 3, Springer, 2006.
[121] Namgyun Jeong, Hyung Do Choi, Ching-Long Lin, Prediction of Darcy–Forchheimer drag for micro-porous structures of complex geometry using the lattice Boltzmann method, J. Micromech. Microeng. 16 (10) (2006) 2240.
[122] Chukwudi Paul Chukwudozie, Pore-Scale Lattice Boltzmann Simulations of Inertial Flows in Realistic Porous Media: a First Principle Analysis of the Forchheimer Relationship, Louisiana State University and Agricultural & Mechanical College, 2011.
[123] Rasoul Arabjamaloei, Douglas Ruth, Numerical study of inertial effects on permeability of porous media utilizing the lattice Boltzmann method, J. Nat. Gas Sci. Eng. 44 (2017) 22–36.
[124] Johannes Schindelin, Ignacio Arganda-Carreras, Erwin Frise, Verena Kaynig, Mark Longair, Tobias Pietzsch, Stephan Preibisch, Curtis Rueden, Stephan Saalfeld, Benjamin Schmid, et al., Fiji: an open-source platform for biological-image analysis, Nat. Methods 9 (7) (2012) 676–682.
[125] Pablo A. García-Salaberri, Prodip K. Das, Effective transport properties for fuel cells: modeling and experimental characterization, in: Fuel Cells for Transportation: Fundamental Principles and Applications, Elsevier, 2023.
[126] Charles Tai-Chieh Wan, Rémy Richard Jacquemond, Yet-Ming Chiang, Kitty Nijmeijer, Fikile R. Brushett, Antoni Forner-Cuenca, Non-solvent induced phase separation enables designer redox flow battery electrodes, Adv. Mater. 33 (16) (2021) 2006716.
[127] Mahmoud Mohammed Gomaa, Arturo Sánchez-Ramos, Nieves Ureña, María Teresa Pérez-Prior Belen Levenfeld, Pablo A. García-Salaberri, Mohamed Rabeh Mohamed Elsharkawy, Characterization and modeling of free volume and ionic conduction in multiblock copolymer proton exchange membranes, Polymers 14 (9) (2022) 1688.
[128] Carl Chan, Nada Zamel, Xianguo Li, Jun Shen, Experimental measurement of effective diffusion coefficient of gas diffusion layer/microporous layer in pem fuel cells, Electrochim. Acta 65 (2012) 13–21.
[129] Xiaoxian Zhang, Yuan Gao, Hossein Ostadi, Kyle Jiang, Rui Chen, Modelling water intrusion and oxygen diffusion in a reconstructed microporous layer of pem fuel cells, Int. J. Hydrog. Energy 39 (30) (2014) 17222–17230.
[130] Mehdi Andisheh-Tadbir, Mohamed El Hannach, Erik Kjeang, Majid Bahrami, An analytical relationship for calculating the effective diffusivity of micro-porous layers, Int. J. Hydrog. Energy 40 (32) (2015) 10242–10250.
[131] M. Sepe, P. Satjaritanun, I.V. Zenyuk, N. Tippayawong, S. Shimpalee, The impact of micro porous layer on liquid water evolution inside pemfc using lattice Boltzmann method, J. Electrochem. Soc. 168 (7) (2021) 074507.
[132] P. Satjaritanun, J.W. Weidner, S. Hirano, Z. Lu, Y. Khunatorn, S. Ogawa, S.E. Litster, A.D. Shum, I.V. Zenyuk, S. Shimpalee, Micro-scale analysis of liquid water breakthrough inside gas diffusion layer for pemfc using X-ray computed tomography and lattice Boltzmann method, J. Electrochem. Soc. 164 (11) (2017) E3359.
[133] Christoph Simon, Frédéric Hasché, Hubert A. Gasteiger, Influence of the gas diffusion layer compression on the oxygen transport in pem fuel cells at high water saturation levels, J. Electrochem. Soc. 164 (6) (2017) F591.
[134] Hong Xu, Shinya Nagashima, Hai P. Nguyen, Keisuke Kishita, Federica Marone, Felix N. Büchi, Jens Eller, Temperature dependent water transport mechanism in gas diffusion layers revealed by subsecond operando X-ray tomographic microscopy, J. Power Sources 490 (2021) 229492.
[135] Soowhan Kim, M.M. Mench, Investigation of temperature-driven water transport in polymer electrolyte fuel cell: phase-change-induced flow, J. Electrochem. Soc. 156 (3) (2009) B353.
[136] Matthew D.R. Kok, Alia Khalifa, Jeff T. Gostick, Multiphysics simulation of the flow battery cathode: cell architecture and electrode optimization, J. Electrochem. Soc. 163 (7) (2016) A1408.
[137] Meysam Heydari Gharahcheshmeh, Charles Tai-Chieh Wan, Yasser Ashraf Gandomi, Katharine V. Greco, Antoni Forner-Cuenca, Yet-Ming Chiang, Fikile R. Brushett, Karen K. Gleason, Ultrathin conformal ocvd pedot coatings on carbon electrodes enable improved performance of redox flow batteries, Adv. Mater. Interfaces 7 (20) (2020) 2000855.
[138] Maxime van der Heijden, Marit Kroese, Zandrie Borneman, Antoni Forner-Cuenca, Investigating mass transfer relationships in stereolithography 3d printed electrodes for redox flow batteries, 2023.
[139] Matthew D.R. Kok, Rhodri Jervis, Tom G. Tranter, Mohammad A. Sadeghi, Dan J.L. Brett, Paul R. Shearing, Jeff T. Gostick, Mass transfer in fibrous media with varying anisotropy for flow battery electrodes: direct numerical simulations with 3d X-ray computed tomography, Chem. Eng. Sci. 196 (2019) 104–115.
[140] Maik Becker, Thomas Turek, New mass transport correlation for vanadium redox-flow batteries based on a model-assisted parameter estimation, Batteries 9 (5) (2023) 253.
[141] Jungmyung Kim, Heesung Park, Recent advances in porous electrodes for vanadium redox flow batteries in grid-scale energy storage systems: a mass transfer perspective, J. Power Sources 545 (2022) 231904.
[142] Vanesa Muñoz-Perales, Pablo Ángel García-Salaberri, Adrian Mularczyk, Santiago Enrique Ibáñez, Marcos Vera, Antoni Forner-Cuenca, Investigating the coupled influence of flow fields and porous electrodes on redox flow battery performance, 2023.

[143] Vanesa Muñoz-Perales, Maxime van der Heijden, Pablo Ángel García-Salaberri, Marcos Vera Coello, Antoni Forner-Cuenca, Engineering lung-inspired flow field geometries for redox flow batteries with stereolithography 3d printing, 2023.

[144] Xi Xu, Yong Hao Tan, Jun Ding, Cao Guan, 3d printing of next-generation electrochemical energy storage devices: from multiscale to multimaterial, Energy Environ. Mater. 5 (2) (2022) 427–438.

[145] Mayank Sabharwal, Lalit M. Pant, Nilay Patel, Marc Secanell, Computational analysis of gas transport in fuel cell catalyst layer under dry and partially saturated conditions, J. Electrochem. Soc. 166 (7) (2019) F3065.

[146] Weibo Zheng, Seung Hyun Kim, The effects of catalyst layer microstructure and water saturation on the effective diffusivity in pemfc, J. Electrochem. Soc. 165 (7) (2018) F468.

[147] Gen Inoue, Kouji Yokoyama, Junpei Ooyama, Takeshi Terao, Tomomi Tokunaga, Norio Kubo, Motoaki Kawase, Theoretical examination of effective oxygen diffusion coefficient and electrical conductivity of polymer electrolyte fuel cell porous components, J. Power Sources 327 (2016) 610–621.

[148] Dinesh C. Sabarirajan, Jiangjin Liu, Yongzhen Qi, Andrea Perego, Andrew T. Haug, Iryna V. Zenyuk, Determining proton transport in pseudo catalyst layers using hydrogen pump dc and ac techniques, J. Electrochem. Soc. 167 (8) (2020) 084521.

[149] Takahisa Suzuki, Hajime Murata, Tatsuya Hatanaka, Yu Morimoto, Analysis of the catalyst layer of polymer electrolyte fuel cells, R&D Review of Toyota CRDL, 39 (3), 2003.

[150] Devproshad K. Paul, Richard McCreery, Kunal Karan, Proton transport property in supported nafion nanothin films by electrochemical impedance spectroscopy, J. Electrochem. Soc. 161 (14) (2014) F1395.

[151] Miguel A. Modestino, Devproshad K. Paul, Shudipto Dishari, Stephanie A. Petrina, Frances I. Allen, Michael A. Hickner, Kunal Karan, Rachel A. Segalman, Adam Z. Weber, Self-assembly and transport limitations in confined nafion films, Macromolecules 46 (3) (2013) 867–873.

[152] Jeff T. Gostick, Adam Z. Weber, Resistor-network modeling of ionic conduction in polymer electrolytes, Electrochim. Acta 179 (2015) 137–145.

[153] Gen Inoue, Motoaki Kawase, Effect of porous structure of catalyst layer on effective oxygen diffusion coefficient in polymer electrolyte fuel cell, J. Power Sources 327 (2016) 1–10.

[154] Julio J. Conde, M. Antonia Folgado, P. Ferreira-Aparicio, Antonio M. Chaparro, Anamika Chowdhury, Ahmet Kusoglu, David Cullen, Adam Z. Weber, Mass-transport properties of electrosprayed pt/c catalyst layers for polymer-electrolyte fuel cells, J. Power Sources 427 (2019) 250–259.

[155] Yuxiu Liu, Michael W. Murphy, Daniel R. Baker, Wenbin Gu, Chunxin Ji, Jacob Jorne, Hubert A. Gasteiger, Proton conduction and oxygen reduction kinetics in pem fuel cell cathodes: effects of ionomer-to-carbon ratio and relative humidity, J. Electrochem. Soc. 156 (8) (2009) B970.

[156] Shaojun Dou, Liang Hao, Hong Liu, Effects of liquid water on the pore structure and transport coefficients in the cathode catalyst layer of pem fuel cells, Int. J. Hydrog. Energy 47 (97) (2022) 41138–41153.

[157] Ahmet Kusoglu, Adam Z. Weber, New insights into perfluorinated sulfonic-acid ionomers, Chem. Rev. 117 (3) (2017) 987–1104.

[158] Thibaut Colinart, S. Didierjean, Olivier Lottin, Gaël Maranzana, C. Moyne, Transport in pfsa membranes, J. Electrochem. Soc. 155 (3) (2008) B244.

[159] Xuemei Wu, Xiaowen Wang, Gaohong He, Jay Benziger, Differences in water sorption and proton conductivity between nafion and speek, J. Polym. Sci., Part B, Polym. Phys. 49 (20) (2011) 1437–1445.

[160] Gert Dorenbos, Yoshinori Suga, Simulation of equivalent weight dependence of nafion morphologies and predicted trends regarding water diffusion, J. Membr. Sci. 330 (1–2) (2009) 5–20.

[161] G. Daniel Sanchez, Alfredo Ortiz, K. Andreas Friedrich, Oscillation of pefc under low cathode humidification: effect of gravitation and bipolar plate design, J. Electrochem. Soc. 160 (6) (2013) F636.

[162] Daniel G. Sanchez, Tiziana Ruiu, Indro Biswas, Mathias Schulze, Stefan Helmly, K. Andreas Friedrich, Local impact of humidification on degradation in polymer electrolyte fuel cells, J. Power Sources 352 (2017) 42–55.

[163] P.A. García-Salaberri, D.G. Sánchez, Pierre Boillat, Marcos Vera, K. Andreas Friedrich, Hydration and dehydration cycles in polymer electrolyte fuel cells operated with wet anode and dry cathode feed: a neutron imaging and modeling study, J. Power Sources 359 (2017) 634–655.

[164] Chi Hoon Park, So Young Lee, Doo Sung Hwang Dong Won Shin, Doo Hee Cho, Kang Hyuck Lee, Tae-Woo Kim, Tae-Wuk Kim, Mokwon Lee, Deok-Soo Kim, et al., Nanocrack-regulated self-humidifying membranes, Nature 532 (7600) (2016) 480–483.

[165] Bei Zhang, Ying Cao, Zhen Li, Hong Wu, Yongheng Yin Li Cao, Xueyi He, Zhongyi Jiang, Proton exchange nanohybrid membranes with high phosphotungstic acid loading within metal-organic frameworks for pemfc applications, Electrochim. Acta 240 (2017) 186–194.

[166] Jiale Chen, Li Wang, Lei Wang, Highly conductive polybenzimidazole membranes at low phosphoric acid uptake with excellent fuel cell performances by constructing long-range continuous proton transport channels using a metal–organic framework (uio-66), ACS Appl. Mater. Interfaces 12 (37) (2020) 41350–41358.

[167] Junrui Li, Haolin Tang, Lutang Chen, Rui Chen, Mu Pan, et al., Highly ordered and periodic mesoporous nafion membranes via colloidal silica mediated self-assembly for fuel cells, Chem. Commun. 49 (58) (2013) 6537–6539.